Quantitative assessment of mitochondrial morphology relevant for studies on cellular health and environmental toxicity

Sophie Charrasse, Titouan Poquillon, Charlotte Saint-Omer, Manuela Pastore, Benoit Bordignon, Richard E Frye, Christelle Reynes, Victor Racine, Abdel Aouacheria

HAL Id: hal-04274749
https://hal.umontpellier.fr/hal-04274749

Submitted on 8 Nov 2023

1 **Quantitative assessment of mitochondrial morphology relevant for studies on cellular health and**

2 **environmental toxicity**

3 Sophie Charrasse[1], Titouan Poquillon[1, 2], Charlotte Saint-Omer[1], Manuela Pastore[3], Benoit Bordignon[4],

4 Richard E Frye[5], Christelle Reynes[3,6], Victor Racine[2] and Abdel Aouacheria[1,†]

5

6 [1] Institut des Sciences de l'Evolution de Montpellier (ISEM, UMR 5554, CNRS/UM/IRD/EPHE),

7 Université de Montpellier, Montpellier, France

8 [2] QuantaCell SAS, Hôpital Saint Eloi, IRMB, 80 avenue Augustin Fliche, 34090 Montpellier, France

9 [3] STATABIO BioCampus, Univ. Montpellier, CNRS, INSERM, Montpellier, France

10 [4] MRI, Montpellier Ressources Imagerie, BioCampus, University of Montpellier, CNRS, INSERM,

11 Montpellier, France

12 [5] Autism Discovery and Treatment Foundation, Phoenix AZ, USA

13 [6] IGF, Univ. Montpellier, CNRS, INSERM, Montpellier, France

14

15

16 Corresponding author:

17 Abdel Aouacheria[†]

18 Institut des Sciences de l'Evolution de Montpellier (ISEM, UMR 5554, CNRS/UM/IRD/EPHE),

19 Université de Montpellier, Montpellier, France

20 Email address: abdel.aouacheria@umontpellier.fr

21

22

23
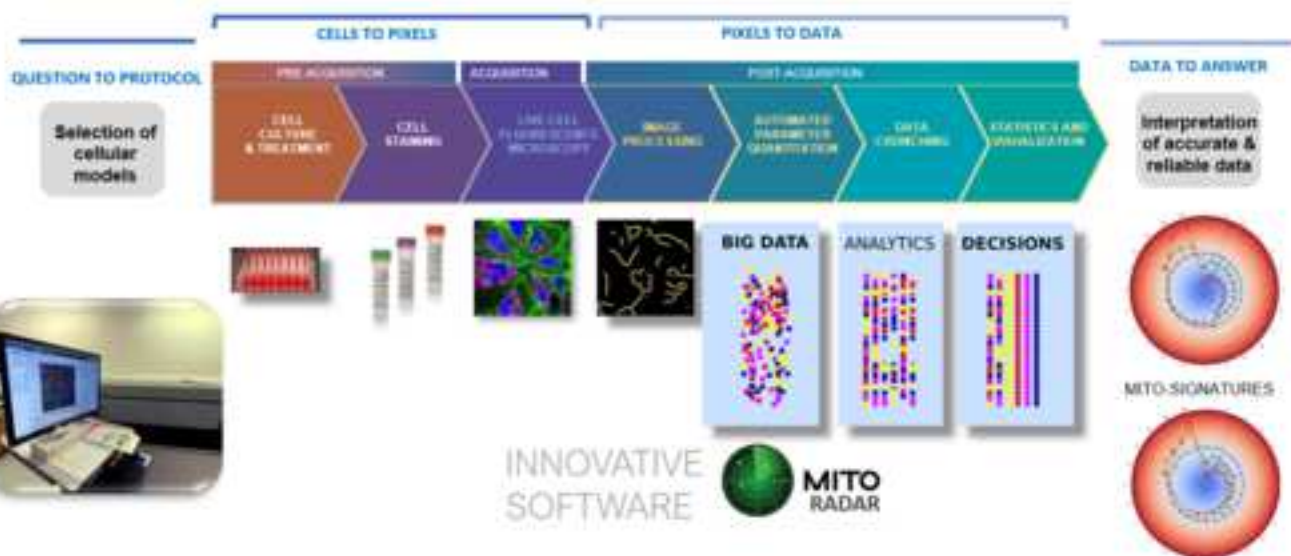
24 Abstract (250 words)

25 Mitochondria are essential organelles that play crucial roles in cellular energy metabolism, calcium

26 signaling and apoptosis. Their importance in tissue homeostasis and stress responses, combined to their

27 ability to transition between various structural and functional states, make them excellent organelles for

28 monitoring cellular health. Quantitative assessment of mitochondrial morphology can therefore provide

29 valuable insights into environmentally-induced cell damage.

30 High-content screening (HCS) provides a powerful tool for analyzing organelles and cellular

31 substructures. We developed a fully automated and miniaturized HCS wet-plus-dry pipeline

32 (MITOMATICS) exploiting mitochondrial morphology as a marker for monitoring cellular health or

33 damage. MITOMATICS uses an in-house, proprietary software (MitoRadar) to enable fast, exhaustive

34 and cost-effective analysis of mitochondrial morphology and its inherent diversity in live cells.

35 We applied our pipeline and big data analytics software to assess the mitotoxicity of selected chemicals,

36 using the mitochondrial uncoupler CCCP as an internal control. Six different pesticides (inhibiting

37 complexes I, II and III of the mitochondrial respiratory chain) were tested as individual compounds and

38 five other pesticides present locally in Occitanie (Southern France) were assessed in combination to

39 determine acute mitotoxicity. Our results show that the assayed pesticides exhibit specific signatures

40 when used as single compounds or chemical mixtures and that they function synergistically to impact

41 mitochondrial architecture.

42 Study of environment-induced mitochondrial damage has the potential to open new fields in

43 mechanistic toxicology, currently underexplored by regulatory toxicology and exposome research.

44 Such exploration could inform health policy guidelines and foster pharmacological intervention, water,

45 air and soil pollution control and food safety.

2

49 Short title

50 Quantitative imaging and phenotyping of mitochondria for toxicity studies.

51

1. Introduction

Mitochondria play a vital role in ATP production and in many critical cellular processes (1,2). Mitochondrial markers are among the first to change upon homeostasis disruption, such as when cells are exposed to environmental stress (3–5) (e.g. toxicants), and during disease (6,7) and aging (8). By sensing and responding to changes in the cellular environment, mitochondria orchestrate adaptive responses that extends well over cellular boundaries to impact tissue, organ and ultimately organism physiology (9). The importance of mitochondria in tissue homeostasis, stress responses and diseases, combined to their ability to transition between various structural and functional states, make them excellent organelles for monitoring cell health (10).

Healthy mitochondria are usually mobile, tubular and interconnected, whereas cells under stress or entering apoptosis often display swollen or fragmented mitochondria, marked by concurrent disruption of metabolism and excess production of reactive oxygen species (ROS) (11). Mitochondrial change in shape and size depending on their functional status, for example going though cycles of fission and fusion to improve mitochondrial quality (12). Thus, mitochondrial morphological phenotypes are complex and heterogeneous. The morphological diversity of this highly dynamic organelle varies from small punctate structures to well-developed reticular networks with numerous intermediate states in-between. To define or classify mitochondrial (network) architectures, only a few terms are usually used, such as *short*, *long*, *fragmented*, *interconnected*, *tubular*, *ramified*, *compacted*, *aggregated*, *dislocated*, *fissioned* or *hyperfused* (13–15). These terms are often used in an operator-dependent, subjective way.

In recent years, to address the challenge of describing this inherent mitochondrial diversity more objectively, several approaches which apply image processing algorithms and morphometric methods have been developed (16–18), providing valuable insights into tissue physiology, pathology and damage (19–21). However, most of these programs are difficult to utilize in standard biology laboratories since they require extensively trained staff and only handle the morphological computation steps, with no visual display, statistical analysis or decision-making support. In most cases, only a limited number of cells or conditions are analyzed with such software, creating ambiguity about the robustness of the obtained data and ultimately as to the true utility of such software.

4

79   Over the last few years, we developed a sophisticated and innovative pipeline (MITOMATICS)

80   exploiting mitochondrial morphology as a marker for monitoring cellular health or damage.

81   MITOMATICS uses computerized methods to enable accurate, fast and cost-effective analysis of

82   mitochondrial shape and network architecture from confocal fluorescent images acquired from cultured

83   living cells. Three successive versions of this in-house, proprietary software were produced: MitoShape

84   (2 shape descriptors) (22), MitoTouch (31 descriptors) (Charrasse et al., submitted) and the here within

85   described MitoRadar (104 shape descriptors). This software is easy to use and does not require any

86   special skills in computer science or image processing. In contrast to previous versions, numerous

87   parameters have been added to provide a multiscale analysis of the mitochondrial component (from

88   solitary mitochondria to mitochondrial clusters present within single cells or in a cell population) and

89   the segmentation step is now performed by deep learning, enhancing image quality and enabling

90   accurate analysis. As a result, MitoRadar generates specific 'mito-signatures', some of which signal

91   cell safety whereas others may provide early predictors of cell danger. In the present study, we applied

92   MitoRadar in the context of predictive and environmental toxicology by assessing mitochondrial

93   architecture in live human cells exposed to specific chemicals, including pesticides used alone or in

94   combination.

95

2. Materials and methods

2.1.1.Chemicals

98   Dimethyl sulfoxide (DMSO; CAS number 67-68-5), Carbonyl cyanide m-chlorophenyl hydrazone

99   (CCCP; CAS number 555-60-2), Rotenone (CAS number 83-79-4), Antimycine A (CAS number 1397-

100   94-0), Mitochondrial Division Inhibitor MDIVI-1 (CAS number 338967-87-6), Mitochondrial Fusion

101   Promoter M1 (CAS number 219315-22-7), Fenpyroximate (CAS number 134098-61-6), Pyridaben

102   (CAS number 96489-71-3), Mepronil (CAS number 55814-41-0), Thifluzamide (CAS number 130000-

103   40-7), Azoxystrobin (CAS number 131860-33-8), Pyraclostrobin (CAS number 175013-18-0), Folpet

104   (CAS number 133-07-3), Pendimathaline, Chlorpyriphos-Methyl (CAS number 5598-13-0), Lindane

5

105 (CAS number 58-89-9), Cyprodinil (CAS number 121552-61-2) were purchased from Sigma Aldrich.

106 Stock solutions between 2 and 100 mM were made in DMSO and stored at -20°C until use. Treatment

107 solutions were prepared freshly for each experiment with a final concentration of DMSO below 0.5 %

108 (v/v) in culture medium.

109 *2.1.2. Cell culture and treatments*

110 A549 (CCL-185), RPE-1 (CRL-4000), U2OS (CRL-3455), Hs68 (CRL-1635), MDA-MB-231 (HTB-

111 26), THLE-3 (CRL-11233), HK-2 (CRL-2190) and BEAS-2B (CRL-9482) cell lines were purchased

112 from ATCC (American Type Culture Collection, LGC, Germany) and cultured in a 5% CO_2 atmosphere

113 at 37°C according to ATCC recommendations. To increase the susceptibility of cells to mitochondrial

114 toxicants, culture medium was replaced by freshly prepared glucose-free medium supplemented with

115 10mM galactose. For treatment, indicated concentrations of chemicals were added to the culture

116 medium. LD50 was determined by counting nuclei 24h after drug exposure. Four biological replicates

117 were performed for all experiments and each experiment was repeated at least 3 times. For the

118 *MitoCocktail* experiments, the most prominent pesticides were tested at concentrations from 10 to

119 500µM and solutions were prepared according to a rule of conservative ratios, i.e., by mixing different

120 pesticides with relative proportions (expressed in µM) based on the ATMO report (where pesticide

121 concentrations are expressed as ng of substance per m^3 of air).

122 *2.1.3. Cell staining and HCS Imaging*

123 A total number of 20,000 to 40,000 cells were seeded onto 96-well black polystyrene microplates

124 (CLS3603, Corning®) 24 to 48h prior conducting experiments. Mitochondrial morphology was

125 examined after staining with 250 nM MitoTracker Deep Red FM (M22426) diluted in phenol red-free

126 culture medium in presence of 2.5 µg/mL Hoechst 33342 (H21492) for 30 min at 37°C. Cells were then

127 washed twice with PBS and labelled with 6.25 µg/mL CellMask Green Plasma Membrane Stain

128 (C37608) for 5 min at 37°C. All these vital dyes were purchased from Thermofisher Scientific (Life

129 Technologies SAS, Courtaboeuf, France). Mitochondrial network, nuclei and membranes of live cells

130 were imaged using the Opera Phenix® High-Content Screening System (PerkinElmer Inc.). Confocal

131 image acquisition (spinning disk) was performed using a 63x water immersion lens (1.15NA LD C-

132 Apochromat) and 5 fields were imaged per well. Automated image capture on a 16bit sCMOS camera

133 (pixel 6.5 μm) using 640 nm/488 nm/405 nm lasers in the indicated order, with Phenix emission filters

134 650-760 nm/500-550 nm/435-550 nm, has been optimized to provide high image quality and resolution.

135 In particular, laser power and exposure time were adjusted to maximize signal without saturation and

136 to minimize photobleaching and background noise (20% power, 100 ms for the far-red channel, 80%

137 power, 500 ms for the green channel and 100%, 200 ms for the blue channel).

2.1.4. Quantification of mitochondrial parameters using MitoRadar

139 As described below, the MitoRadar software (APP deposit number: IDDN.FR.001.470036

140 .000.S.P.2022.000.31235) consists of several modules designed for data handling, data processing,

141 detection and comprehensive analysis of mitochondrial changes in HCS imaging data.

2.1.5. Basic image import and processing

143 First, a loading module enables the import of fluorescence images from high-content imaging (HCI)

144 microscopes. A plate module can be used to add experimental data information during the loading stage.

145 A data handling module allows for the sorting of images and assignment of plate data, well data, and

146 experimental data. It can also be used to add and update experimental data information at any time

147 during the analysis process.

148 The segmentation module of MitoRadar uses deep learning and state-of-the-art image processing

149 techniques to detect cells, nuclei and mitochondria in HCS images (Fig. S1 A) at various scales (Fig.

150 S1 B). The MitoRadar segmentation technique utilizes a tri-channel fluorescence image input with

151 different colors associated to nuclei, mitochondria and cytoplasm. In this study, 2160x2160 images

152 were analyzed at a resolution of 94nm.pix-1 (Fig. S1 C panel a).

153 Next, both nucleus and cell channels undergo a normalization process between 0 and 1 utilizing a

154 quantile normalization approach between quantile 1% and quantile 99%. A trained convolutional

155 network (Cellpose uNet) (23,24) is applied to each channel to perform instance segmentation of cell

156 and nuclei. The uNet produces a probability map and a gradient flow which enables the reconstruction

157 of object instances. This method was proven to be effective for cell segmentation of objects with

158 irregular shapes (25–27). To reduce computation time, the images are down-sampled to 224 pixels

159 before entering the neural network and are up-sampled post-analysis using nearest neighbors followed

160 by a median filtering technique to smooth edges (Fig. S1 C panel b). The nuclei instances are then

161 associated with cells utilizing a 1-to-1 association rule, with the greater intersection size used to resolve

162 conflicts when necessary (Fig. S1 C panel c).

163 Due to variations in mitochondrial intensity between cells within the same field, mitochondrial

164 segmentation is performed cell by cell following the segmentation of nuclei and cells. The

165 corresponding bounding box within the mitochondrial channel is extracted for each cell, and the average

166 intensity inside the cell mask is utilized for background noise removal. The intensities are normalized

167 between 0 and 1 utilizing a quantile normalization approach between quantile 0% and quantile 99.9%.

168 Next, a Gaussian difference threshold (sigma=0.9 µm, t=0.05) and a Laplacian of Gaussian threshold

169 (sigma=0.9 µm, t=0) are applied to produce a mitochondrial mask for the cell. Clusters are defined as

170 connected components on this mask (Fig. S1 C panel d) and are refined by removing small objects (size

171 < 16 pixels or 0.13 µm²) followed by morphological closing. The skeletons of mitochondrial clusters

172 are extracted utilizing Zhang's algorithm (28) (Fig. S1 C panel e). Finally, to detect each individual

173 instance of mitochondria, a watershed approach is applied to mitochondrial intensities using the

174 skeleton branches as seeds and the mitochondrial mask as the mask (Fig. S1 C panel f). Moreover, this

175 segmentation module can be parallelized and utilizes the GPU for fast processing of a large number of

176 images.

177 *2.1.6.Automated parameter quantification with integrated statistics*

178 After segmentation, pictures are declumped and a quantification module then collects 104

179 morphological, intensity and texture parameters (hereby referred to as 'morphological descriptors'; see

180 Table S1 for the exhaustive list and further details) on cells, nuclei, mitochondria and mitochondrial

181 clusters. These descriptors can be used to characterize various aspects of mitochondrial architecture,

182 such as size, shape, density and organization within the cellular area. Note that the current version of

183 the software does not normalize descriptor values based on the cell size. Finally, the analysis module

8

184 of MitoRadar allows users to make state-of-the-art statistical tests and plots on the resulting

185 quantifications and to easily compare experimental conditions. This module also includes integrated

186 linear discriminant analysis (LDA) and principal component analysis (PCA) for exploring multivariate

187 effects and a specific MitoRadar plot to access both significance and amplitude information.

188 The MitoRadar analysis module can calculate a MitoScore based on a cross validation of the impact

189 (difference with the basal condition) and number of all affected parameters. First, a hierarchical

190 clustering is applied to remove redundancies among descriptors. Then, 20 LDA models are trained on

191 50% fold random samples of the data to differentiate between the control and the trial conditions. These

192 are then tested on the complementary folds using the average balanced accuracy between all LDA

193 models as a score showing how easily a ML algorithm can discriminate between control and trial. The

194 top 15 significant uncorrelated descriptors that discriminate the compared conditions are then shown in

195 a MitoRadar plot and a slider is placed along a heat color scale, leading to the delineation of five distinct

196 categories (*No effect, Limited / Substantial / Measurable* or *Large overall effect*) (Fig.1).

197

3. Results

3.1.1.Design of the MITOMATICS workflow

200 Quantitative imaging of cellular structures and substructures like mitochondria requires rethinking low-

201 throughput experimental procedures to include the use of multi-well plates (rather than tissue culture

202 petri dishes or small imaging chambers), live cell techniques (instead of fixed-cell imaging methods),

203 random imaging of multiple fields (rather than operator-dependent monitoring of only one chosen

204 microscope field encompassing multiple cells), databases of high-quality, classified images (rather than

205 production of a limited number of acquired images), automated digital image processing (instead of

206 manual counting) and rapid, massive data gathering, analysis and visualization (rather than slow

207 performance data analysis with suboptimal charts, graphs or histograms hindering easy and correct data

208 interpretation). The MITOMATICS wet-plus-dry pipeline has been specifically designed for high-

209 throughput phenotyping of mitochondrial morphology by miniaturizing and automating high-resolution

210 imaging before an in-house software application (MitoRadar) handles all fundamental operations from

211 image segmentation to statistical analysis and drawing meaningful interpretation from custom mito-

212 signatures (Fig. 1). The use of 96-well plates with random imaging of 5 fields per well enables analysis

213 of multiple experimental conditions while achieving robust results. To image mitochondria in their

214 cellular context, we use the potentiometric dye MitoTracker Deep Red (MTDR) in combination with

215 fluorescent markers (green and blue, respectively) specific for cellular membranes (Cell Mask Green)

216 and nuclei (Hoechst 33342). Confocal images are acquired on an Opera Phenix® High-Content

217 Screening (HCS) System (equipped in its optimal configuration with a robotic arm and incubator) and

218 directly loaded into the MitoRadar software to perform the post-acquisition steps. This software uses

219 deep learning during the image segmentation phase (Fig. S1) and calculates about a hundred

220 morphological descriptors (Table S1), offering one of the most comprehensive sets of parameters to

221 infer mitochondrial (network) shape and overall cell morphology. The MitoRadar software enables the

222 detection and assessment of subtle morphological characteristics, undetectable or barely detectable

223 through conventional methods and has advanced analytical, statistical and graphical features for data

224 representation, analysis and interpretation. Our miniaturized technology suits diverse applications

225 among which are: testing the noxious effect of individual molecules on the mitochondrial network

226 (*MitoCollapse* module for predictive toxicology) ; testing the deleterious effects of combinations of

227 molecules, drugs or pollutants (*MitoCocktail* module for predictive as well as environmental

228 toxicology) ; assessing changes in mitochondrial morphology in pathological (or aged) cells compared

229 to their non-pathological (or 'young') counterparts (*MitoMedCare* module) and objectifying the

230 beneficial effects of cosmetic or pharmacological bioactive ingredients (*MitOasis* module) (Fig. 1). In

231 the present report, we focus only on the first two applications.

232

3.1.2. Implementation of the MitoRadar software

234 Here, we sought to validate our fully automated image analysis pipeline on rich datasets gathered from

235 cultured live human cells exposed to specific chemicals known to induce either mitochondrial

236 fragmentation (CCCP, Rot, Ant A) (29–32) or mitochondrial hyperfusion (MDIVI-1, M1) (33,34).

10

237 Eight human cell lines of normal and diseased states, from different tissue origin, were successfully

238 imaged (Fig. S2), leading to an image database of approximately 30,000 microphotographs (named

239 'MITOPIX-DEV', DEV standing for 'development') that was used to develop the MitoRadar software.

240 Representative images are shown in Fig. 2 for BEAS-2B cells (see Fig. S3 for the other cell lines), a

241 human lung epithelial cell line that has been widely used in toxicity tests, specifically to assess the

242 deleterious effects of heavy metals (35), microplastics (36), fine particles (37) and pesticides (38).

243 Based on MITOPIX-DEV, the MitoRadar software was implemented, optimized and extensively

244 debugged over a six-month period. Several functionalities were implemented: (i) an AI image

245 segmentation module (using deep learning) to detect cells, nuclei and mitochondria (Fig 3A, 3B panel

246 a and Fig. S1 A); (ii) a quantification module to characterize the detected objects with advanced

247 descriptors (n=104, see Table S1 for the exhaustive list); note that for each descriptor, 4 distribution

248 aggregators were computed: mean, variance, skewness and kurtosis, allowing for a more refined and

249 realistic description of the objects under study; (iii) a database with its dedicated interface dynamically

250 linking the data and metadata of the experiments (Fig. 3B panel b); and finally (iv) an interface for

251 integrated analysis (including statistics) and easy visualization of the results (Fig. 3B panels c-d and

252 Fig. 3C).

253 MitoRadar provides a comprehensive analysis of the morphological characteristics of the

254 mitochondriome of cells by performing morphometric measurements at the supra-mitochondrial,

255 mitochondrial and sub-mitochondrial levels. The computer program is multiscalar, allowing to navigate

256 over a diverse range of scales (isolated mitochondria, clusters of mitochondria, subcellular locations,

257 cells, cell cultures) (Fig. S1B) and multidimensional, multivariate quantitative data being readily

258 visualizable through innovative radar charts. Each variable is represented along the X-axis. The

259 computed parameters are compared to a reference situation (blue circle) and parameters showing

260 statistically significant deviation are displayed along a heat map Y-axis (the size of the points along the

261 curve reflecting the degree of statistical significance). Six different MitoRadar plots can be created by

262 grouping the parameters associated with single or networked mitochondria, the total mitochondrial

263 complement present in a given cell (mitochondriome), cellular features, nuclear features and attributes

11

of the *counter shape* (i.e., inverted selection of the cellular region containing labelled mitochondria, to our best knowledge this latter category of descriptors being completely new in the field) (see Fig. 3C). Parameters that show little or no variation compared to the control are listed in brown, those that decrease or increase are respectively colored in blue and red, with fixed rank ordering or (according to user preference) with a rank assigned in descending or ascending order.

Results are generated in the form of reports of decreasing complexity, integrating statistical analysis and advanced graphical representation tools (two functionalities absent from most image analysis software, which require separate manual processing by a trained operator). The colors and their intensities are correlated with the size of the measured effects, and statistical significance is represented by circles of increasing diameter (Fig. 3C). The user can choose between PCA, LDA, correlation map or dendrogram, T-Test with corrections for multiple comparisons, and SSMD (Fig. 3B panels c-d). All of these advanced statistical tests are natively integrated into MitoRadar's user-friendly graphical interface, which makes them accessible without any third-party software to biologists who do not have programming skills. It also makes it easy to share projects, images, and quantifications.

3.1.3. MitoRadar validation on high-throughput microscopy images of cells treated with the mitochondrial uncoupler CCCP

During cellular stress when ROS accumulates the mitochondrial network becomes largely fragmented (39). CCCP, an inhibitor of mitochondrial oxidative phosphorylation, evokes the integrated stress response and its application to cells results in dramatic fragmentation of mitochondria (29,30). To test the performance of MitoRadar as a big data analytics software, we treated BEAS-2B cells with 20µM CCCP during 4h (Fig. 4A). Five independent experiments were done with more than 200,000 cells analyzed, representing about 32,580 microphotographs and a total processing time of around 260 minutes (for the whole project). The three upper MitoRadar plots of Fig. 4B show a massive and highly significant variation of more than 90% of the descriptors (55/61) related to the mitochondrial phenotype, most of them (47) with $p < 0.001***$ (Mann Whitney Test with Benjamini Hochberg correction). Among

the descriptors that decrease (in blue) and account for size reduction of both mitochondria and mitochondrial (sub)networks, we find area_mean, aspect_ratio_mean, axis_major_length_mean and axis_minor_length_mean, equivalent_diameter_area_mean, feret_diameter_max_mean and perimeter_crofton_mean.

Mitochondrial fragmentation is evidenced by the augmentation (in red) of circularity and roundness. Smaller degrees of mitochondrial interconnection and branching are evidenced by the decrease in skeleton length and number of branch points (skel_length_mean, branch_points_mean, clusterised_mito and clustering_coef). Consistent with this dislocation of the mitochondrial reticulum, the number of mitochondria and specifically of isolated mitochondria appears greater. Texture as well as density profiles undergo concomitant variations as indicated by increase in solidity_mean and in Euler number means, which relate to the number of holes in the analyzed cells when mitochondria and mitochondrial clusters are considered (Fig. 4B, top right panels) and in their inferred negative shapes or *countershape* (Fig. 4B, bottom middle panel). Subcellular distribution of the mitochondria also reflects cellular stress as shown by their positioning away from the cell membrane and closer to the nucleus.

Compared to mitochondrial parameters, changes in cellular parameters are less drastic (Fig. 4B, bottom right plot) and suggest slight spreading of the cells. Because the set of nuclear parameters (n=18) does not display any significant change at all (Fig. 4B, bottom left plot), our data demonstrate that MitoRadar objectively measures mitochondria-damaging effects before the onset of early apoptotic features (such as the appearance of highly condensed pyknotic nuclei, cell shrinking and blebbing). These mitochondria-damaging effects are described as 'large' by an in-house scoring system, MitoScore (Fig. 4C), which comprises a color-coded scale and a summary of the most affected parameters (see *Methods* for details).

MitoRadar software natively offers a range of both basic and fairly advanced statistical tools for data analysis, such as PCA, LDA and violin plots (i.e., hybrids of box plots and kernel density plots) (Fig. 4D). Details on SSMD values (Fig. S4 A), u-values (Fig. S4 B) and p-values (Fig. S4 C) were also plotted separately for better clarity (readability) and counting of u-values. Lastly, note that

13

mitochondrial descriptors show a high level of correlation on both correlation dendrogram (or hierarchical clustering diagram) (Fig. S4 D) and distance map (Fig. S4 E), revealing a global transformation of the mitochondrial component. The PCA plot shows that the control and CCCP conditions clearly segregate into two distinct groups (Fig. 4D, panel a). Projection of the descriptors onto the axes of the PCA confirms that the observed variations are mainly due to changes in mitochondrial features (Fig. S4 F). LDA with prior knowledge of class labels improves the observed segregation between the control and CCCP-treated groups (Fig. 4D, panel b and Fig. S4 G). Violin plots are useful for plotting variations in individual descriptors as exemplified here by the Mito roundness_mean variable (Fig. 4D, panel c). Altogether, our results suggest that MitoRadar operates quickly, efficiently, reliably and cost-effectively to distinguish a highly fragmented mitochondrial network from a normal, healthy one using live-cell fluorescence microscopy images of cultured mammalian cells.

3.1.4.MitoCollapse: assessing acute mitochondrio-toxicity of single pesticides in vitro

Exposure to anthropogenic pollutants is a critical biomedical and ecological issue, pesticides being potentially hazardous to human health and one of the main contributors to environmental deterioration. We hypothesized that our approach could be useful to assess the in vitro mitochondrial toxicity of a selection of pesticides, taking CCCP as an internal positive control of cell poisoning. Four different fungicides were chosen, including the two ETC complex II inhibitors Mepronil (MEP) and Thifluzamide (THI) as well as Azoxystrobin (AZO) and Pyraclostrobin (PYRA), which are two ETC complex III inhibitors, plus the two acaricides Fenpyroximate (FEN) and Pyridaben (PYRI), which are ETC complex I inhibitors.

Pulmonary BEAS-2B cells were treated with various concentrations (10, 50, 100, 250 and 500 μM) of individual pesticides and images were taken 2h after pesticide exposure. The threshold dose (i.e., the dose below which MitoRadar plots show no variation compared to control) and LD50 (i.e, the dose for which 50% of cells died 24h after) were then evaluated (Fig 5A). MitoRadar analysis corresponding to

14

343 features obtained with the 250μM dose (Fig. 5B) showed a clear disruption of mitochondria and their

344 networks in cells following single pesticide treatment, compared to control cells, resulting into a

345 MitoScore transitioning from '*Substantial overall effect*' to '*Large overall effect*' (Fig. 5C).

346 Like CCCP, all of these pesticides appeared to trigger mitochondrial fragmentation when applied at a

347 dose of 250μM, MitoRadar plots showing an increase in the circularity_mean, roundness_mean, and

348 isolated_mito parameters with concomitant decrease in skel_length_mean, area_mean,

349 axis_major_length_mean and axis_minor_length_mean.

350 Interestingly, analysis with MitoRadar also revealed several unexpected differences between the

351 measured effects of the various pesticides. For example, average length of the minor axis of

352 mitochondria decreased after treatment with CCCP, THI and PYRA, while a significant increase was

353 observed for this parameter with the other pesticides. Likewise, the number of mitochondria was

354 increased for CCCP as well MET and THI (inhibitors of complex II) and decreased for AZO and PYRA

355 (inhibitors of complex III). When LDA was carried out on defined pairs of pesticides according to their

356 type of ETC inhibition, untreated controls were well separated from the defined groups (as well as from

357 the CCCP-treated group) by the first two discriminant axis (Fig. 5D).

358 Compared to the negative control (vehicle), the Mito euler_number_mean, which reflects the number

359 of holes in the mitochondrial network, was smaller for the group of Complex III inhibitors, followed by

360 Complex II and I inhibitors, while skeleton length values progressively decreased with ETC inhibitors

361 I, III and II.

362 Nuclear parameters related to size tended to increase for CCCP while they decreased significantly for

363 PYRA. Few variations of the cell and countershape features were detected as shown on the MitoRadar

364 plots (Fig. S5 A). Details of the statistical analyses are presented in Fig. S5 (correlation distance MAP

365 Fig. S5 B; SSMD summary Fig. S5 C; U-Value Fig. S5 D).

366 Therefore, although as a first approximation the mitochondrial response to the tested single toxicants

367 was assumed to be similar (with pesticide treatment resulting in mitochondrial fragmentation), using

368 built-in statistical analysis modules, MitoRadar analysis was able to reveal subtle changes in the deep

369 architecture of mitochondrial structures.

370

3.1.5. MitoCocktail: assessing acute mitochondrio-toxicity of pesticide mixtures in vitro

372 We took advantage of MITOMATICS for assessing the mitochondrial toxicity of pesticides

373 administered in combination on cultured BEAS-2B cells, according to real-world data (40) produced

374 by ATMO-Occitanie, the accredited association for air quality monitoring in the Occitanie Region

375 (France). Annual campaigns to measure pesticides in the ambient air have been carried out over 12

376 months since 2014 in a rural environment dominated by wine, arboriculture or field crops. Based on the

377 cumulative concentrations of the fifteen most commonly found pesticide residues in the different

378 departments of Occitanie (Tarn-et-Garonne, Pyrénées-Orientales, Lauragais, Aude and Gard), the top

379 five air-borne pesticides were selected for further analysis. The list of pesticides under study comprised

380 two fungicides, Folpel (FOL) and Cyprodinil (CYP), one herbicide, Pendimethaline (PEN) and two

381 insecticides, Lindane (LIN, banned since 1998) and Chlorpyriphos methyl (CHL) (Fig. 6A).

382 First, these five pesticides were tested separately (as above) on BEAS-2B cells for 4h at various

383 concentrations ranging from 10 to 500 µM to determine the threshold dose. After 24h, the number of

384 cells was recorded in each condition and the LD50 was calculated. A summary of the results from 4

385 independent experiments (representing about 100,000 analyzed cells) is presented in Fig. 6A.

386 Next, to determine if the pesticides can be more noxious when combined (a phenomenon known as the

387 'cocktail effect'), we prepared mixtures with relative proportions of pesticides based on the ATMO

388 report. Note that the identity of the most prominent pesticide (which was tested at concentrations

389 ranging from 10 to 500µM) varied across departments, representing between 78% and 97% of the final

390 mixture (Fig. 6B).

391 Our data indicate that both the threshold dose and the acute LD50 of pesticide mixtures were at least

392 five times lower than that of individual pesticides in all considered departments (Fig. 6A and B). The

393 case of Aude is taken here as an illustration. In this department, FOL is the main air-borne pesticide

16

394 (97%), whereas the three other pesticides (PEN, CHL and LIN) are present as traces (in the following

395 proportions: 1.1%, 0.8% and 1.5%, respectively).

396 Mitochondrial disorganization was observable microscopically (Fig. 6C) and measurable through

397 MitoRadar analysis (Fig. 6D) when 10μM FOL was mixed with low concentrations of the other

398 pesticides (0.11μM PEN; 0.15μM CHL and 0.08μM LIN), i.e., when each individual pesticide was

399 present at levels below its "no-observed-effect-concentration" (threshold doses were 50μM for FOL;

400 >500μM for PEN; 100μM for CHL and 500μM for LIN).

401 The computed MitoScore (based on the top 15 most affected parameters) indicated weak to moderate

402 effects when cells were exposed to single pesticides at a 10μM concentration and maximal noxious

403 effect with the pesticide mixture (Fig. 6E). In conclusion, traces of PEN, CHL and LIN potentiate both

404 the mitochondrial and cellular toxicity of FOL. Note that similar conclusions can be drawn for the

405 pesticide combinations characteristic of the other four departments.

406

407 4. Discussion

408 Mitochondria are membrane-enclosed organelles ubiquitously found in eukaryotes. Originally derived

409 from endosymbiotic bacteria, they play a vital role in energy production and in many other cellular

410 functions (2,41). It is considered that all physicochemical, parasitic and microbial influences that

411 surround eukaryotic life are translated into changes in mitochondrial structure and function (42–47). In

412 particular, a growing body of literature points to mitochondria as a key organelle targeted by

413 environmental pollutants (3–5,48–53). Not only do these environmental pollutants (present in air, water

414 and soil) disturb the mitochondrial machinery but their mitotoxicity may cause significant damage to

415 the epigenome and transgenerational inheritance of dysfunctional mitochondria (4). Mitochondria are

416 thus considered to provide the missing link between cellular, organismal and environmental health (10).

417 As 'mitochondrial form follows function' (54), previous studies highlighted the utility of using

418 mitochondrial morphology as a proxy for monitoring cell health and cytotoxicity (17,46,55–59). In this

419 paper, we described a comprehensive and user-friendly big data analytics software (MitoRadar)

17

420 combined with a HCS wet pipeline (MITOMATICS) to analyze mitochondrial shape changes occurring

421 in live cultured cells. We applied our image-based phenotypic profiling system to assess mitochondrial

422 architecture in response to environmental pollutants. This system was designed to replace traditional,

423 costly and low-throughput techniques, which will be reserved for downstream validation on prioritized

424 combinations.

425 Because mitochondrial changes appear to happen before other cellular events, shorter incubation

426 durations are needed, this approach thus saves time and money while enhancing efficiency. While most

427 available tools require programming experience or computer science skills, the core component of our

428 workflow involves an easy-to-work-with and intuitive in-house, proprietary software (MitoRadar).

429 Live-cell, high-resolution confocal images are collected on any multiplexed imaging platforms

430 available and from any type of cells cultured on 96-well plates and stained with different vital dyes

431 (with one of them labelling mitochondria), before processing of a large number of images at various

432 possible scales, AI-driven segmentation and automatic calculation by MitoRadar of 2D descriptors

433 associated with the identified mitochondria in their cellular context.

434 By quickly computing more than one hundred descriptors related to mitochondria (some of which being

435 novel like the '*Countershape*') and additional nuclear and cellular shape parameters, MitoRadar

436 represents one of the most comprehensive software packages available for image analysis. Our

437 automated and miniaturized approach integrates a convenient way for interpreting the gathered massive

438 and multidimensional data by creating unique radar plots in which sample datasets (e.g. from cells

439 treated with chemicals) are compared to a reference dataset (i.e., untreated or mock-treated cells). These

440 information-rich representations natively come up with a variety of statistical charts and plots (t-tests,

441 PCA, LDA, violin distributions) and with a simple score (MitoScore), making it quick and easy to

442 compare the impact of various substances or culture conditions and to detect subtle morpho-phenotypic

443 variations. It is remarkable that our method was able to discriminate the effect of molecules acting at

444 different stages of mitochondrial function, namely CCCP (a widely used mitochondrial uncoupler),

445 Rotenone (Complex I inhibitor) and Antimycin (Complex III inhibitor). Besides CCCP and other

446 traditional uncouplers (like FCCP or 2,4-dinitrophenol), novel mitochondria-specific uncoupling agents

18

447 such as BAM15 and FR58P1 (60) or the organic pollutant pentachlorophenol (61) were identified that

448 could be tested using our technology to improve our knowledge of the consequences of mitochondrial

449 uncoupling on mitochondrial network architecture. In addition to Antimycin A, which is specific to the

450 N-side quinone binding site of Complex III, it would be interesting to assess the effects of Myxothiazol,

451 which acts at the P-side. Inhibitors of Complex IV (potassium cyanide, sodium azide or lipophilic small

452 molecules like steroids) and ATP synthase inhibitors like oligomycin and dicyclohexylcarbodiimide

453 (DCCD), which respectively bind to the F_O and F_OF_1 subunits of the proton pump, are also worth testing.

454 Here, we applied our technology to test the noxious potential of single pollutants (*MitoCollapse*) as well

455 as combination effects between molecules (*MitoCocktail*).

456 Regarding *MitoCollapse*, we recently collected results on single exposure of skin cells to three

457 pesticides (two insecticides, fipronil and imidacloprid as well as glyphosate, present in the widely used

458 herbicide Roundup®) (Charrasse et al. submitted) and, in the present study, of non-tumorigenic lung

459 cells to eleven additional pesticides including five currently detected in Occitanie (Southern France).

460 This research is in line with classic toxicology studies carried out by various organizations such as the

461 National Institute of Environmental Health Sciences through its National Toxicology Program (NTP).

462 Interestingly, the mitochondrial 'morpho-signatures' of the six chemicals that we tested so far as

463 individual substances appear not only to be distinct but also to segregate into discrete families,

464 suggesting that the effects of pesticides (and virtually of any environmental pollutant(s)) might be

465 classified within a 'morphospace' of mitochondriome morphologies. It would be interesting to

466 determine whether specific signatures are linked to particular physicochemical properties of pesticides

467 or to their toxicological profile.

468 The combined effects of chemical mixtures, a rapidly emerging topic in environmental toxicology (62),

469 prompted us to design another module, *MitoCocktail*, for estimating the mitochondrial response of a

470 larger number of substances, across a battery of concentrations and in combination. This functionality

471 currently handles projects using a single dose response of combined drugs, rather than a full two-way

472 matrix of varying doses, similar to other HCS studies. Mixture effects are usually classified as being

473 antagonistic, additive or synergistic, depending on whether the observed toxicity of the combination is

19

474 lower than, equal to, or higher than the expected toxicity based on an additivity model. Thanks to

475 pollutant data made available by ATMO-Occitanie, we showed that the deleterious effects on

476 mitochondrial architecture and cellular viability of the main pesticide found in each department of

477 Occitanie were enhanced when trace quantities of other pesticides were added, indicative of

478 synergistic relationships.

479 MitoRadar analysis can help decipher human health impacts of anthropogenic chemicals found in the

480 air, but also in water, food and soil. In addition to pesticides, various sources of pollution can be studied,

481 such as fine particles, polycyclic aromatic hydrocarbons, plastics, pharmaceutical waste, cosmetics and

482 even antibiotics (63) or noise pollution (64). Samples taken from natural environments and containing

483 unidentified pollutants or metabolites may also be blind tested. Beyond exposure to pollutants, other

484 variables may be considered such as genetic or epigenetic contexts, age, disease, diet and physical

485 exercise that are likely to influence mitochondrial health. Our method is also suitable for analyzing

486 primary cells from different organs or tissues of patients with particular life histories, such as for

487 instance type 2 diabetes (65) or autism spectrum disorder (66), in order to gain better understanding of

488 the mitochondrial correlates of pathophysiology. In that respect, it would be of interest to assay the

489 morphometric parameters of mitochondria in cell lines derived from children with autistic disorder (in

490 comparison to paired cells lines from typically developing siblings or control cell lines) with or without

491 exposure to environmental factors such as air pollution or pesticides (67–70). This is indeed very

492 relevant to this population as studies have shown changes in mitochondrial respiration with exposure to

493 toxicants such as air pollution (69) and other common toxicants (71) in children with autism. This

494 technique could be applied to disease populations to understand how environmental agents may produce

495 disease through effects on bioenergetics. Taking up the One Health perspective (72,73), non-

496 mammalian cell lines may also be tested including honeybee or zebrafish cell lines. Indeed, several

497 pesticides (e.g. succinate dehydrogenase inhibitors, SDHIs) that are toxic to mitochondria act by

498 blocking cellular respiration. This property, used to eliminate certain fungi, mites or worms, makes

499 them potentially toxic for all living beings.

The MITOMATICS technology can be combined with phenotypic/functional analysis (e.g. measurement of mitochondrial activities through ELISA plate readers and spectrophotometric methods, determination of apoptosis/necrosis rates by flow cytometry) and followed by more specialized readouts including measuring oxygen consumption and extracellular acidification rates (using Seahorse®), mitochondrial iron content through biochemical techniques or the uptake of specific fluorescent probes (like DCFH-DA for detecting ROS) by flow cytometry or fluorescent imaging. For example, in a recent study (66), mitochondrial morphology paralleled variations in respiratory rates in fibroblasts derived from patients and healthy controls, thereby allowing the validation of the respiratory changes and a better understanding of the consequence of these changes in mitochondrial respiration.

Our approach may be improved in a number of ways. In particular, the mitochondriome should be viewed as a four-dimensional architecture (X,Y,Z + time) whose configuration may evolve due to mitochondrial fission, fusion and motility as well as cell movements (including various extension of the cell surface, migration and division). Albeit non-amenable to HCS screening, future MITOMATICS developments will use bioimaging techniques that could capture mitochondria in 4D, such as lattice light-sheet microscopy (LLSM) and three-dimensional structured illumination microscopy (3D SIM). For now, our method for 2D automated quantification of mitochondrial morphology appears to be well-suited for relatively 'flat' cells, i.e., cells where mitochondria are confined to a limited number of planes. Utilization of cells cultured in 3D (through different systems including spheroids, hydrogels or scaffolds) could improve physiological relevance for certain cell types (like endothelial cells or mixed cell populations such as in 3D reconstituted skin) or conditions (e.g. growth of cancer cells).

5. Conclusions

In vitro assessment of mitochondrial toxicity through our novel quantitative imaging system can be useful to draft prioritized lists of deleterious chemicals, ranked according to their impact on mitochondria, before functional tests and in vivo assays are conducted. Our HCS system may also serve as a valuable tool to transition from the current single-chemical-based risk paradigm towards one which addresses co-exposures to multiple chemicals, and more generally to multiple stressors due to external exposome and/or pathological conditions.

21

8. References

1. Nunnari J, Suomalainen A. Mitochondria: in sickness and in health. Cell. 2012 Mar 16;148(6):1145–59.

2. Monzel AS, Enríquez JA, Picard M. Multifaceted mitochondria: moving mitochondrial science beyond function and dysfunction. Nat Metab. 2023 Apr;5(4):546–62.

3. Meyer JN, Hartman JH, Mello DF. Mitochondrial Toxicity. Toxicol Sci. 2018 Mar 1;162(1):15–23.

552   4. Duarte-Hospital C, Tête A, Brial F, Benoit L, Koual M, Tomkiewicz C, et al.
553   Mitochondrial Dysfunction as a Hallmark of Environmental Injury. Cells. 2021 Dec
554   30;11(1):110.

555   5. Reddam A, McLarnan S, Kupsco A. Environmental Chemical Exposures and
556   Mitochondrial Dysfunction: a Review of Recent Literature. Curr Environ Health Rep.
557   2022 Dec;9(4):631–49.

558   6. Luo Y, Ma J, Lu W. The Significance of Mitochondrial Dysfunction in Cancer. Int J Mol
559   Sci. 2020 Aug 5;21(16):5598.

560   7. Frye RE, Lionnard L, Singh I, Karim MA, Chajra H, Frechet M, et al. Mitochondrial
561   morphology is associated with respiratory chain uncoupling in autism spectrum disorder.
562   Transl Psychiatry. 2021 Oct 13;11(1):527.

563   8. Bornstein R, Gonzalez B, Johnson SC. Mitochondrial pathways in human health and
564   aging. Mitochondrion. 2020 Sep;54:72–84.

565   9. Aouacheria A, Baghdiguian S, Lamb HM, Huska JD, Pineda FJ, Hardwick JM.
566   Connecting mitochondrial dynamics and life-or-death events via Bcl-2 family proteins.
567   Neurochem Int. 2017 Oct;109:141–61.

568   10. Naviaux RK. Perspective: Cell danger response Biology-The new science that connects
569   environmental health with mitochondria and the rising tide of chronic illness.
570   Mitochondrion. 2020 Mar;51:40–5.

571   11. Friedman JR, Nunnari J. Mitochondrial form and function. Nature. 2014 Jan
572   16;505(7483):335–43.

573   12. Sprenger HG, Langer T. The Good and the Bad of Mitochondrial Breakups. Trends Cell
574   Biol. 2019 Nov;29(11):888–900.

575   13. Leonard AP, Cameron RB, Speiser JL, Wolf BJ, Peterson YK, Schnellmann RG, et al.
576   Quantitative analysis of mitochondrial morphology and membrane potential in living
577   cells using high-content imaging, machine learning, and morphological binning. Biochim
578   Biophys Acta. 2015 Feb;1853(2):348–60.

579   14. Peng JY, Lin CC, Chen YJ, Kao LS, Liu YC, Chou CC, et al. Automatic morphological
580   subtyping reveals new roles of caspases in mitochondrial dynamics. PLoS Comput Biol.
581   2011 Oct;7(10):e1002212.

582   15. Reis Y, Bernardo-Faura M, Richter D, Wolf T, Brors B, Hamacher-Brady A, et al. Multi-
583   parametric analysis and modeling of relationships between mitochondrial morphology
584   and apoptosis. PLoS One. 2012;7(1):e28694.

585   16. Harwig MC, Viana MP, Egner JM, Harwig JJ, Widlansky ME, Rafelski SM, et al.
586   Methods for imaging mammalian mitochondrial morphology: A prospective on
587   MitoGraph. Anal Biochem. 2018 Jul 1;552:81–99.

588   17. Zahedi A, On V, Phandthong R, Chaili A, Remark G, Bhanu B, et al. Deep Analysis of
589   Mitochondria and Cell Health Using Machine Learning. Sci Rep. 2018 Nov
590   5;8(1):16354.

23

591   18. Rohani A, Kashatus JA, Sessions DT, Sharmin S, Kashatus DF. Mito Hacker: a set of
592   tools to enable high-throughput analysis of mitochondrial network morphology. Sci Rep.
593   2020 Nov 3;10(1):18941.

594   19. Ahmad T, Aggarwal K, Pattnaik B, Mukherjee S, Sethi T, Tiwari BK, et al.
595   Computational classification of mitochondrial shapes reflects stress and redox state. Cell
596   Death Dis. 2013 Jan 17;4(1):e461.

597   20. Hemmerich J, Troger F, Füzi B, F Ecker G. Using Machine Learning Methods and
598   Structural Alerts for Prediction of Mitochondrial Toxicity. Mol Inform. 2020
599   May;39(5):e2000005.

600   21. Giedt RJ, Fumene Feruglio P, Pathania D, Yang KS, Kilcoyne A, Vinegoni C, et al.
601   Computational imaging reveals mitochondrial morphology as a biomarker of cancer
602   phenotype and drug response. Sci Rep. 2016 Sep 9;6:32985.

603   22. Jugé R, Breugnot J, Da Silva C, Bordes S, Closs B, Aouacheria A. Quantification and
604   Characterization of UVB-Induced Mitochondrial Fragmentation in Normal Primary
605   Human Keratinocytes. Sci Rep. 2016 Oct 12;6:35065.

606   23. Stringer C, Wang T, Michaelos M, Pachitariu M. Cellpose: a generalist algorithm for
607   cellular segmentation. Nat Methods. 2021 Jan;18(1):100–6.

608   24. Ronneberger O, Fischer P, Brox T. U-Net: Convolutional Networks for Biomedical
609   Image Segmentation. In: Navab N, Hornegger J, Wells WM, Frangi AF, editors. Medical
610   Image Computing and Computer-Assisted Intervention – MICCAI 2015 [Internet].
611   Cham: Springer International Publishing; 2015 [cited 2023 Sep 16]. p. 234–41. (Lecture
612   Notes in Computer Science; vol. 9351). Available from:
613   http://link.springer.com/10.1007/978-3-319-24574-4_28

614   25. Kromp F, Fischer L, Bozsaky E, Ambros IM, Dorr W, Beiske K, et al. Evaluation of
615   Deep Learning Architectures for Complex Immunofluorescence Nuclear Image
616   Segmentation. IEEE Trans Med Imaging. 2021 Jul;40(7):1934–49.

617   26. Waisman A, Norris AM, Elías Costa M, Kopinke D. Automatic and unbiased
618   segmentation and quantification of myofibers in skeletal muscle. Sci Rep. 2021 Jun
619   3;11(1):11793.

620   27. Pachitariu M, Stringer C. Cellpose 2.0: how to train your own model. Nat Methods. 2022
621   Dec;19(12):1634–41.

622   28. Zhang TY, Suen CY. A fast parallel algorithm for thinning digital patterns. Commun
623   ACM. 1984 Mar;27(3):236–9.

624   29. Ishihara N, Jofuku A, Eura Y, Mihara K. Regulation of mitochondrial morphology by
625   membrane potential, and DRP1-dependent division and FZO1-dependent fusion reaction
626   in mammalian cells. Biochem Biophys Res Commun. 2003 Feb 21;301(4):891–8.

627   30. Miyazono Y, Hirashima S, Ishihara N, Kusukawa J, Nakamura KI, Ohta K. Uncoupled
628   mitochondria quickly shorten along their long axis to form indented spheroids, instead of
629   rings, in a fission-independent manner. Sci Rep. 2018 Jan 10;8(1):350.

31. Leonard AP, Cameron RB, Speiser JL, Wolf BJ, Peterson YK, Schnellmann RG, et al. Quantitative analysis of mitochondrial morphology and membrane potential in living cells using high-content imaging, machine learning, and morphological binning. Biochim Biophys Acta. 2015 Feb;1853(2):348–60.

32. Tauber J, Dlasková A, Šantorová J, Smolková K, Alán L, Špaček T, et al. Distribution of mitochondrial nucleoids upon mitochondrial network fragmentation and network reintegration in HEPG2 cells. Int J Biochem Cell Biol. 2013 Mar;45(3):593–603.

33. Maneechote C, Chattipakorn SC, Chattipakorn N. Recent Advances in Mitochondrial Fission/Fusion-Targeted Therapy in Doxorubicin-Induced Cardiotoxicity. Pharmaceutics. 2023 Apr 7;15(4):1182.

34. Maneechote C, Chattipakorn SC, Chattipakorn N. Recent Advances in Mitochondrial Fission/Fusion-Targeted Therapy in Doxorubicin-Induced Cardiotoxicity. Pharmaceutics. 2023 Apr 7;15(4):1182.

35. Cao X, Fu M, Bi R, Zheng X, Fu B, Tian S, et al. Cadmium induced BEAS-2B cells apoptosis and mitochondria damage via MAPK signaling pathway. Chemosphere. 2021 Jan;263:128346.

36. Dong CD, Chen CW, Chen YC, Chen HH, Lee JS, Lin CH. Polystyrene microplastic particles: In vitro pulmonary toxicity assessment. J Hazard Mater. 2020 Mar 5;385:121575.

37. Sotty J, Kluza J, De Sousa C, Tardivel M, Anthérieu S, Alleman LY, et al. Mitochondrial alterations triggered by repeated exposure to fine (PM2.5-0.18) and quasi-ultrafine (PM0.18) fractions of ambient particulate matter. Environ Int. 2020 Sep;142:105830.

38. Kanno S, Hirano S, Mukai T, Ro A, Kato H, Fukuta M, et al. Cellular uptake of paraquat determines subsequent toxicity including mitochondrial damage in lung epithelial cells. Leg Med (Tokyo). 2019 Mar;37:7–14.

39. Perdiz D, Oziol L, Poüs C. Early mitochondrial fragmentation is a potential in vitro biomarker of environmental stress. Chemosphere. 2019 May;223:577–87.

40. Langevine A. La lettre de l'Air n°19 [Internet]. Atmo Occitanie, observatoire régional de l'air; 2022. Available from: https://www.atmo-occitanie.org/sites/default/files/publications/2022-03/Lettre%20de%20l%27air%20n%C2%B019%20La%20surveillance%20des%20pesticides%20dans%20l%27air%20en%202019-20.pdf

41. Roger AJ, Muñoz-Gómez SA, Kamikawa R. The Origin and Diversification of Mitochondria. Curr Biol. 2017 Nov 6;27(21):R1177–92.

42. Wan X, Garg NJ. Sirtuin Control of Mitochondrial Dysfunction, Oxidative Stress, and Inflammation in Chagas Disease Models. Front Cell Infect Microbiol. 2021;11:693051.

43. Wang Y, Li N, Zhang X, Horng T. Mitochondrial metabolism regulates macrophage biology. J Biol Chem. 2021 Jul;297(1):100904.

25

668 44. Nunnari J, Suomalainen A. Mitochondria: in sickness and in health. Cell. 2012 Mar
669   16;148(6):1145–59.

670 45. Bornstein R, Gonzalez B, Johnson SC. Mitochondrial pathways in human health and
671   aging. Mitochondrion. 2020 Sep;54:72–84.

672 46. Aouacheria A, Baghdiguian S, Lamb HM, Huska JD, Pineda FJ, Hardwick JM.
673   Connecting mitochondrial dynamics and life-or-death events via Bcl-2 family proteins.
674   Neurochem Int. 2017 Oct;109:141–61.

675 47. Friedman JR, Nunnari J. Mitochondrial form and function. Nature. 2014 Jan
676   16;505(7483):335–43.

677 48. Strilbyska OM, Tsiumpala SA, Kozachyshyn II, Strutynska T, Burdyliuk N, Lushchak
678   VI, et al. The effects of low-toxic herbicide Roundup and glyphosate on mitochondria.
679   EXCLI J. 2022;21:183–96.

680 49. Ferramosca A, Lorenzetti S, Di Giacomo M, Murrieri F, Coppola L, Zara V. Herbicides
681   glyphosate and glufosinate ammonium negatively affect human sperm mitochondria
682   respiration efficiency. Reprod Toxicol. 2021 Jan;99:48–55.

683 50. Pereira SP, Santos SMA, Fernandes MAS, Deus CM, Martins JD, Pedroso de Lima MC,
684   et al. Improving pollutants environmental risk assessment using a multi model toxicity
685   determination with in vitro, bacterial, animal and plant model systems: The case of the
686   herbicide alachlor. Environ Pollut. 2021 Oct 1;286:117239.

687 51. Peters A, Nawrot TS, Baccarelli AA. Hallmarks of environmental insults. Cell. 2021 Mar
688   18;184(6):1455–68.

689 52. Lim S, Ahn SY, Song IC, Chung MH, Jang HC, Park KS, et al. Chronic exposure to the
690   herbicide, atrazine, causes mitochondrial dysfunction and insulin resistance. PLoS One.
691   2009;4(4):e5186.

692 53. Xu S, Pi H, Chen Y, Zhang N, Guo P, Lu Y, et al. Cadmium induced Drp1-dependent
693   mitochondrial fragmentation by disturbing calcium homeostasis in its hepatotoxicity. Cell
694   Death Dis. 2013 Mar 14;4(3):e540.

695 54. Wang C, Youle R. Cell biology: Form follows function for mitochondria. Nature. 2016
696   Feb 18;530(7590):288–9.

697 55. Lihavainen E, Mäkelä J, Spelbrink JN, Ribeiro AS. Mytoe: automatic analysis of
698   mitochondrial dynamics. Bioinformatics. 2012 Apr 1;28(7):1050–1.

699 56. Peng JY, Lin CC, Chen YJ, Kao LS, Liu YC, Chou CC, et al. Automatic morphological
700   subtyping reveals new roles of caspases in mitochondrial dynamics. PLoS Comput Biol.
701   2011 Oct;7(10):e1002212.

702 57. Ahmad T, Aggarwal K, Pattnaik B, Mukherjee S, Sethi T, Tiwari BK, et al.
703   Computational classification of mitochondrial shapes reflects stress and redox state. Cell
704   Death Dis. 2013 Jan 17;4(1):e461.

705 58. Vowinckel J, Hartl J, Butler R, Ralser M. MitoLoc: A method for the simultaneous
706   quantification of mitochondrial network morphology and membrane potential in single
707   cells. Mitochondrion. 2015 Sep;24:77–86.

708 59. Valente AJ, Maddalena LA, Robb EL, Moradi F, Stuart JA. A simple ImageJ macro tool
709   for analyzing mitochondrial network morphology in mammalian cell culture. Acta
710   Histochem. 2017 Apr;119(3):315–26.

711 60. Demine S, Renard P, Arnould T. Mitochondrial Uncoupling: A Key Controller of
712   Biological Processes in Physiology and Diseases. Cells. 2019 Jul 30;8(8):795.

713 61. Xia M, Huang R, Shi Q, Boyd WA, Zhao J, Sun N, et al. Comprehensive Analyses and
714   Prioritization of Tox21 10K Chemicals Affecting Mitochondrial Function by in-Depth
715   Mechanistic Studies. Environ Health Perspect. 2018 Jul;126(7):077010.

716 62. Rietdijk J, Aggarwal T, Georgieva P, Lapins M, Carreras-Puigvert J, Spjuth O.
717   Morphological profiling of environmental chemicals enables efficient and untargeted
718   exploration of combination effects. Sci Total Environ. 2022 Aug 1;832:155058.

719 63. Wang X, Ryu D, Houtkooper RH, Auwerx J. Antibiotic use and abuse: a threat to
720   mitochondria and chloroplasts with impact on research, health, and environment.
721   Bioessays. 2015 Oct;37(10):1045–53.

722 64. Zou M, Huang M, Zhang J, Chen R. Exploring the effects and mechanisms of
723   organophosphorus pesticide exposure and hearing loss. Front Public Health.
724   2022;10:1001760.

725 65. Shenouda SM, Widlansky ME, Chen K, Xu G, Holbrook M, Tabit CE, et al. Altered
726   mitochondrial dynamics contributes to endothelial dysfunction in diabetes mellitus.
727   Circulation. 2011 Jul 26;124(4):444–53.

728 66. Frye RE, Lionnard L, Singh I, Karim MA, Chajra H, Frechet M, et al. Mitochondrial
729   morphology is associated with respiratory chain uncoupling in autism spectrum disorder.
730   Transl Psychiatry. 2021 Oct 13;11(1):527.

731 67. Rossignol DA, Genuis SJ, Frye RE. Environmental toxicants and autism spectrum
732   disorders: a systematic review. Transl Psychiatry. 2014 Feb 11;4(2):e360.

733 68. Frye RE, Cakir J, Rose S, Palmer RF, Austin C, Curtin P. Physiological mediators of
734   prenatal environmental influences in autism spectrum disorder. Bioessays. 2021
735   Sep;43(9):e2000307.

736 69. Frye RE, Cakir J, Rose S, Delhey L, Bennuri SC, Tippett M, et al. Prenatal air pollution
737   influences neurodevelopment and behavior in autism spectrum disorder by modulating
738   mitochondrial physiology. Mol Psychiatry. 2021 May;26(5):1561–77.

739 70. Frye RE, Cakir J, Rose S, Palmer RF, Austin C, Curtin P, et al. Mitochondria May
740   Mediate Prenatal Environmental Influences in Autism Spectrum Disorder. J Pers Med.
741   2021 Mar 18;11(3):218.

27

71. Frye RE, Rose S, Wynne R, Bennuri SC, Blossom S, Gilbert KM, et al. Oxidative Stress Challenge Uncovers Trichloroacetaldehyde Hydrate-Induced Mitoplasticity in Autistic and Control Lymphoblastoid Cell Lines. Sci Rep. 2017 Jun 30;7(1):4478.

72. Brack W, Barcelo Culleres D, Boxall ABA, Budzinski H, Castiglioni S, Covaci A, et al. One planet: one health. A call to support the initiative on a global science-policy body on chemicals and waste. Environ Sci Eur. 2022;34(1):21.

73. Humboldt-Dachroeden S, Mantovani A. Assessing Environmental Factors within the One Health Approach. Medicina (Kaunas). 2021 Mar 5;57(3):240.

Legends to Figures

Figure 1.

Overview of the MITOMATICS workflow.

The main steps of automated analysis of mitochondrial morphology using the MITOMATICS workflow are presented. Cellular models are selected (MITOGATE) to assess the mitochondria-disrupting effects of single chemicals (*MitoCollapse*) or of molecules used in combination (*MitoCocktail*). Fluorescent images of live cultured cells with labeled mitochondria are captured and loaded into MitoRadar. The images are segmented and a total of 104 morphological and texture features are extracted for each frame. The values can be plotted for a particular cell or for all cells present in a given microscopic field, at the level of the whole mitochondrial population or for mitochondrial subnetworks. The software handles data analysis, statistics and visual exploration for instance in the form of radar plots. Reference condition is standardized by a blue circle for comparison with a different cellular state (lines with other colors). The basic steps of this wet-plus-dry pipeline are thus as follows: (i) Pre-acquisition steps: cell treatment including culture in 96-well plates, drug exposure and staining. (ii) Acquisition step: live-cell imaging (5 random fields/well) acquired on an Opera Phenix High-Content Screening system (or other imaging platform). (iii) Post-acquisition steps: fully automated image analysis by the MitoRadar software including image processing, AI-driven segmentation, parameter quantification, statistics, visual representation and scoring. Note that the Graphical Abstract shows a differently annotated

28

770 version of the pipeline: the step of cellular model selection corresponds to 'Question to protocol', pre-

771 acquisition and acquisition steps are classed under the denomination 'Cells to pixels' and, lastly, post-

772 acquisition steps are referred to as 'Pixels to Data' and 'Data to Answer'.

773

774 Figure 2.

775 **Implementation of the MITOPIX-DEV image dataset of BEAS-2B cells treated with**

776 **mitochondrial pro-fission and hyper-fusion drugs.**

777 BEAS-2B cells were treated with vehicle (0,5% DMSO), pro-fission drugs (20 μM CCCP, 1 μM

778 Rotenone and 1 μM Antimycin A), and hyper-fusion drugs (50 μM MDIVI-1 and 10 μM M1) for 2h

779 and stained with HOE (blue), CMG dye (green) and MTDR (purple) before confocal imaging (on the

780 Opera Phenix HCS system). Images from the different fluorescent channels are presented separately or

781 merged (overlay). Zoom-ins are shown. Scale bar = 10μm.

782

783 Figure 3.

784 **Overwiew of the MitoRadar software.**

785 (A) MitoRadar main page. The left panel allows users to manage data and launch image processing

786 tasks while the center panel is dedicated to visualization (of both images and segmentation results). The

787 right panel shows the descriptor values and their distribution for a single field or on the whole dataset.

788 (B) MitoRadar basic features: a-Segmentation visualization panel (showing cells, nuclei, mitochondria

789 and skeletons); b-Experimental data import module to link experimental data from the plates to the

790 captured images; c-Advanced statistical panel to produce advanced statistical representations with PCA,

791 LDA, Correlation, T-Test, SSMD and MitoRadar plots; d-Example of a 3D LDA plot produced with

792 MitoRadar in-house statistical module. (C) The resulting data are plotted into MitoRadar charts, where

793 the reference condition is standardized by a blue circle for comparison with another experimental

794 condition of interest (orange line), such as chemical treatment or diseased status. Parameters can be

795 ranked in ascending order according to their SSMD values and they are colored in blue when the effect

796 is diminished, brown when it is low and red when it is increased. Significant differences from basal for

797 each experimental group are depicted by small (*: p<0.05), medium (**: p<0.01) or large (***:

798 p<0.001) circles (Mann Whitney Test).

799

800 Figure 4.

801 **Quantitative analysis of mitochondrial morphology in BEAS-2B cells treated with the**

802 **mitochondrial uncoupler CCCP.**

803 (A) Representative confocal microscopy images of BEAS-2B cells treated with 0,5% DMSO (vehicle,

804 left panel) or 20μM CCCP (right panel) during 4h before mitochondrial staining (with MTDR). Scale

805 bar = 10μm. (B) More than 4,000 CCCP-treated cells were analyzed using the MitoRadar software; the

806 six different MitoRadar plots figure distribution of the normalized 104 morphometric features. The

807 upper three MitoRadar plots correspond to computation for total mitochondria (*Mito*), clustered

808 mitochondria (*Mitocluster*) or *Mitochondriome* (the full mitochondrial pool of a cell, considered as a

809 single object), whereas the bottom three MitoRadar plots result from calculations of *Nuclear*,

810 *Countershape* and cellular characteristics (*Cell*). Descriptors are colored in blue when the measured

811 effect is diminished and in red when it is increased. Significant differences from basal (blue circle) for

812 the CCCP-treated condition (orange line) are depicted by small (*: p<0.05), medium (**: p<0.01) or

813 large (***: p<0.001) circles (Mann Whitney Test). Shown are representative data of n=5 independent

814 experiments. (C) MitoRadar can calculate a MitoScore based on the deviation and number of affected

815 parameters. Top 15 descriptors are listed. (D) Statistical analysis performed by MitoRadar. a- PCA plot

816 on the first two components, with arrows indicating descriptor correlation with each axis; b- Box plot

817 along the unique LDA axis; c- Violin plot showing a particular descriptor: Mito-roundness_mean, as

818 an example.

819

820   Figure 5.

821   **Quantitative analysis of mitochondrial morphology after acute exposure of human pulmonary**

822   **cells to single pesticides (*MitoCollapse*).**

823   (A) List of pesticides tested alone on BEAS-2B cells for 2h at different doses ranging from 10 to 500

824   µM, chemical category, threshold dose inferred by MitoRadar analysis and LD50 determined 24h post-

825   treatment. (B) BEAS-2B cells were treated for 2h with vehicle (0,5% DMSO), 20µM of CCCP or

826   250µM of individual pesticides (FEN, PYRI, MEP, THI, AZO or PYRA). MitoRadar plots (morpho-

827   phenotypic signatures) obtained after analysis by MitoRadar. For statistical analysis, a Mann-Whitney

828   U test was used. Each MitoRadar plot results from analysis of around 20,000 cells and shown data are

829   representative of 4 independent experiments. Note that when Mitoradar plots are computed with data

830   obtained 2h post-treatment with 100µM of THI (**Fig. S6,** grey color), which is the calculated LD50/24h

831   value for this pesticide, changes in parameters indicative of mitochondrial toxicity are already visible

832   (with an increase in roundness_mean, circularity_mean, solidity_mean, compaction_mean and

833   concomitant decrease in area_mean, axis_major_length_mean, axis_minor_length_mean,

834   skel_length_mean). Complete single-compound dose–responses are shown in **Fig. S7**. (C) MitoScore

835   for estimating treatment effect. Shown are the most affected parameters along a color-coded scale with

836   explicit reference to one of the following five categories: *No effect, Limited / Substantial / Measurable*

837   or *Large overall effect*. (D) Bidimensional representation of the established group into the new subspace

838   generated by the first two LDA discriminant axis. Both LDA axis separate samples exposed to ETC

839   complex I, II and III inhibitors and CCCP from the untreated ones.

840

841   Figure 6.

842   **Quantitative analysis of mitochondrial morphology after acute exposure of human pulmonary**

843   **cells to pesticide mixtures (*MitoCocktail*)**

844   (A) List of pesticides tested alone on BEAS-2B cells for 4h at different doses ranging from 10 to 500

845   µM, chemical category, threshold dose inferred by MitoRadar analysis and LD50 determined 24h post-

31

treatment. Data shown are representative of at least 4 independent experiments with 4 replicates per experiment. (B) Table listing the main air-borne pesticides found in the five departments of region Occitanie (Southern France) and their relative percentage (according to real-world data produced by ATMO-Occitanie). The prominent pesticide (in red) detected in each of these five locations was tested at 5 doses ranging from 10 to 500 µM, the other pesticides in the mixture at the dose corresponding to their percentage in each region. The threshold dose inferred by MitoRadar and the LD50 are reported in the third and fourth column of the Table. (C) Representative confocal microscopy images of mitochondria (stained with MTDR) present in BEAS-2B cells after treatment with 0,5% DMSO (panel a), 10µM FOL (panel b), 50µM FOL (panel c) or with a mixture of pesticides found in the Aude department (one of the five departments of region Occitanie) with main pesticide (FOL) concentration set at 10 µM (panel d). (D) MitoRadar plots showing variations in mitochondrial parameters after treatment with vehicle (0,5% DMSO, blue circle), 10µM (orange), 50µM (green) or 100µM (red) of FOL alone (left MitoRadar) or by the mixture of pesticides found in Aude with the main pesticide (FOL) concentration set at 10, 50 or 100µM (respectively in orange, green and red in the right panel). (E) MitoScore for estimating treatment effect. Shown are the most affected parameters along a color-coded scale with explicit reference to one of the following five categories: *No effect, Limited / Substantial / Measurable* or *Large overall effect*.

MitoRadar segmentation module.

(A) Labelled nuclei, membranes and mitochondria are imaged and pictures are loaded into the MitoRadar software. The images are processed through successive segmentation, labelling and transformation steps. For the first segmentation step which consist in detecting cells and nuclei, MitoRadar uses deep learning. Image processing and morphometric measurements are fully automated and can be parallelized. (B) Descriptors pertaining to multiscale (wells /fields /cells / nuclei /

872 mitochondriome / countershape /clusters of mitochondria/ isolated mitochondria) and multidimensional

873 analysis (n=104) for identification of complex phenotypes. (C) Segmentation step (detail). Tri-channel

874 staining (a): cell membranes are labeled in green, nuclei in blue and mitochondria in purple. Cell label

875 (b). Nuclei label (c). Clustered mitochondria label (d). Mitochondrial skeleton label (e). Isolated

876 mitochondria label (f). Note that in our image analysis workflow, images were "down-sampled" only

877 for the nuclei and cytoplasm channels to maximize segmentation efficacy and computational efficiency

878 (these objects being large enough, this operation only minimally affects their definition). Mitochondrial

879 segmentation was carried out at the maximum image resolution (i.e., images were processed at full

880 resolution without any pre-processing step).

881

882

883 Supplementary Table 1 (Table S1).

884 List of descriptors, classification and definition.

885

886 Supplementary Figure 2 (Fig. S2).

887 **Fluorescence imaging of eight human cell lines.**

888 Representative confocal microscopy images of the following cell lines: BEAS-2B (non-tumorigenic

889 lung epithelial cells), A549 (lung adenocarcinoma cells), RPE-1 (retinal pigment epithelial-1 cells),

890 U2OS (osteosarcoma cells), Hs68 (foreskin fibroblasts), THLE-3 (liver epithelial cells), MDA-MB231

891 (triple-negative breast cancer cells) and HK-2 (kidney proximal tubule cells). Nuclei were labelled using

892 Hoechst (blue; HOE), membranes with CellMask dye (green; CMG) and mitochondria with the

893 mitochondria-specific dye MitoTracker Deep Red FM (purple; MTDR). Pictures were taken by live-

894 cell confocal microscopy on the Opera Phenix® HCS system. Images from the different fluorescent

895 channels are presented separately or merged (overlay). N=2 independent experiment with 10 replicates

896 for each condition and more than 10,000 analyzed fields. Zoom-ins are shown. Scale bar = 10µm.

897

Treatment of different human cell lines with mitochondrial pro-fission and hyper-fusion drugs for implementation of the MITOPIX-DEV image dataset.

BEAS-2B, A549, RPE-1, U2OS, Hs68, THLE-3, MDA-MB231 and HK-2 cells were treated with vehicle (DMSO), pro-fission drugs (20 µM CCCP, 1 µM Rotenone and 1 µM Antimycin A), and hyper-fusion drugs (50 µM MDIVI-1 and 10 µM M1) for 2h and stained with HOE (blue), CMG dye and MTDR before confocal imaging (on the Opera Phenix® HCS System). Images from the different fluorescent channels were merged (overlay). Zoom-ins are presented. Scale bar = 10µm.

906

Overview of MitoRadar statistical analysis system (example of CCCP treatment).

(A) Summary of the SSMD based on comparison between control cells (0.5% DMSO, vehicle) and cells treated with a pro-fission drug (20 µM CCCP for 4h). This measure of the size effect is greater between both groups when the square is red, and smaller when the square is blue. (B) and (C) U- and p-value computations using Mann-Whitney test and T-test respectively, plus Benjamini-Hochberg correction. When the difference between the compared groups is statistically significant for a given variable, the squares are labeled in dark green (see for instance Mito_roundness_mean), whereas when the differences are not significant, the squares are labeled in grey (see for instance the whole set of nuclear parameters). (D) Hierarchical clustering of the computed parameters. (E) Correlation distance map showing the dependence between descriptors. Detailed view of the correlation of descriptors along each axis for PCA (F) and LDA (G).

919

MitoRadar analytical platform with advanced statistics.

922 (A) MitoRadar plots showing features associated with nuclei, countershape and cells, after 2h exposure

923 to 250µM of pesticides (FEN in red, PYRI in pink, MEP in violet, THI in grey, AZO in orange and

924 PYRA in brown), 20 µM CCCP (in green) or 0,5% DMSO (blue circle as a reference). (B) Correlation

925 distance map showing dependence between descriptors. (C) SSMD summary showing size effect. (D)

926 U-values computations using Mann-Whitney test and significance level after Benjamini-Hochberg

927 correction.

928

929 Supplementary Figure 6 (Fig. S6)

930 **Quantitative analysis of mitochondrial morphology after acute exposure of human pulmonary**

931 **cells to 100µM of single pesticides.**

932 BEAS-2B cells were treated for 2h with vehicle (0,5% DMSO), 20µM of CCCP or 100µM of

933 individual pesticides (FEN, PYRI, MEP, THI, AZO or PYRA). MitoRadar plots (morpho-

934 phenotypic signatures) obtained after analysis by MitoRadar. For statistical analysis, a Mann-

935 Whitney U-test was used. Each MitoRadar plot results from analysis of around 20,000 cells

936 and shown data are representative of 4 independent experiments.

937

938 Supplementary Figure 7 (Fig. S7)

939 **Quantitative analysis of mitochondrial morphology after acute exposure of human pulmonary**

940 **cells to 10-500µM of single pesticides (dose-reponses).**

941 BEAS-2B cells were treated for 2h with vehicle (0,5% DMSO, blue circle), 20µM of CCCP (pink

942 broken line) or with 10µM (orange), 50 µM (purple), 100µM (green), 250µM (red), or 500µM (brown)

943 of individual pesticides (FEN, PYRI, MEP, THI, AZO or PYRA). MitoRadar plots (morpho-phenotypic

944 signatures) obtained after analysis by MitoRadar. For statistical analysis, a Mann-Whitney U-test was

945 used. Each MitoRadar plot results from analysis of around 20,000 cells and shown data are

946 representative of 4 independent experiments.

Figure 1

Figure 2

Figure 3

Figure 4

Figure 5

A
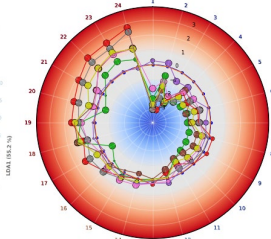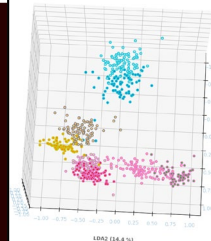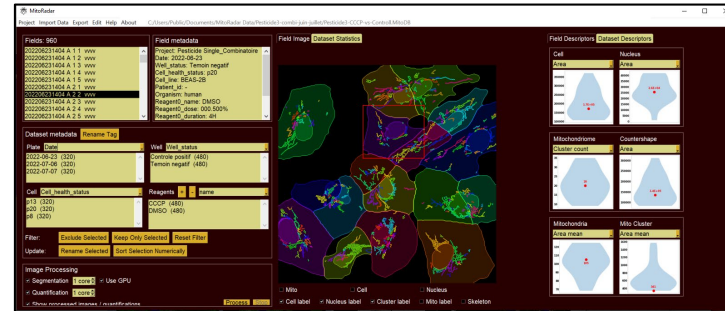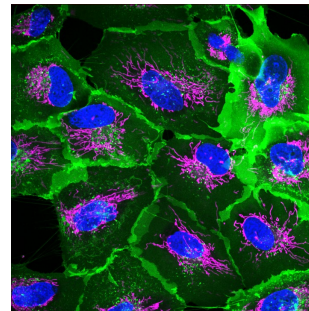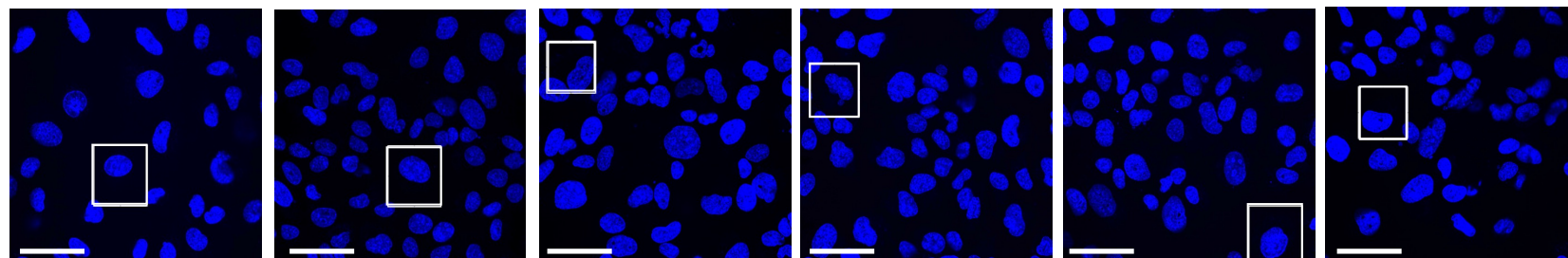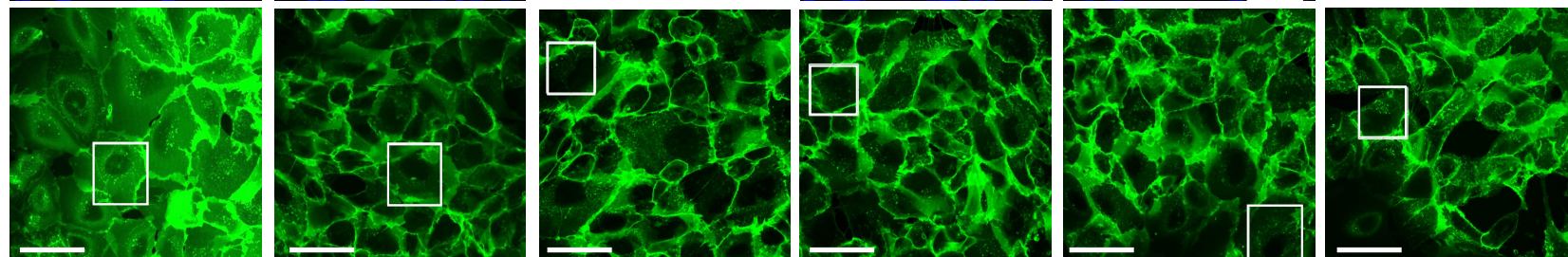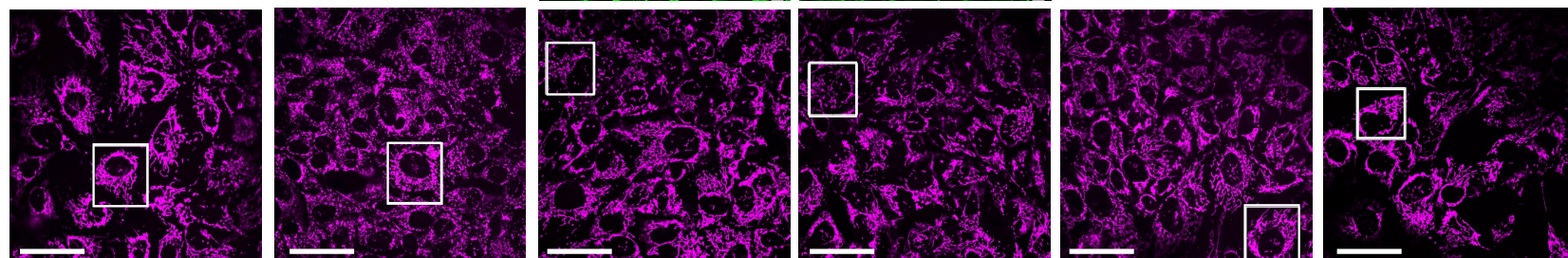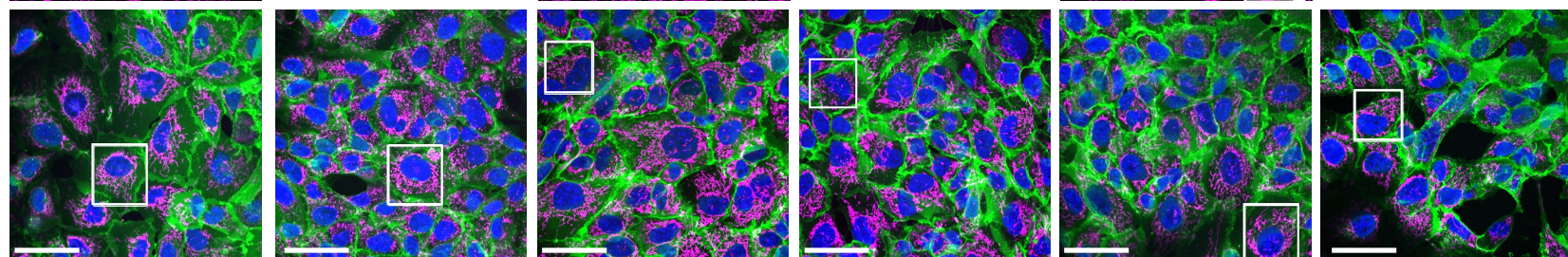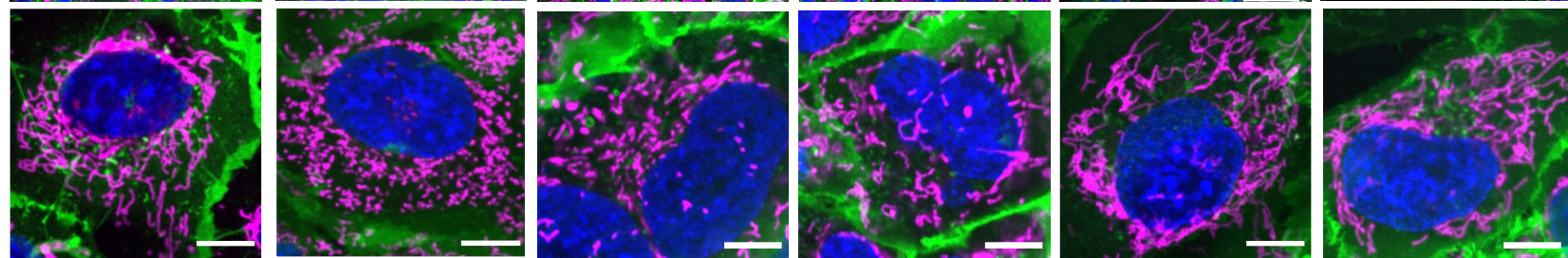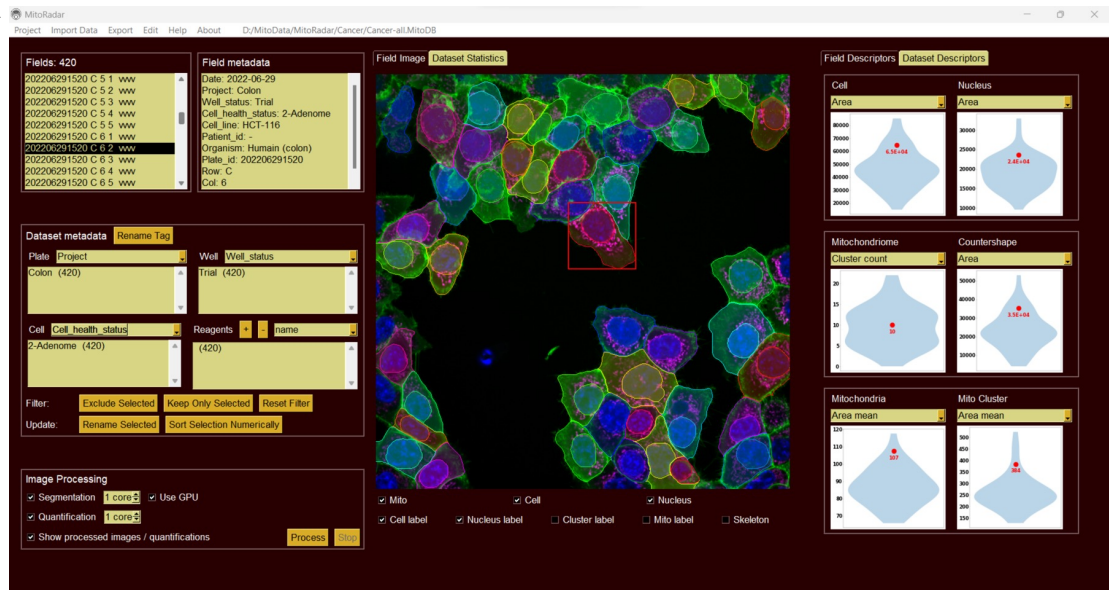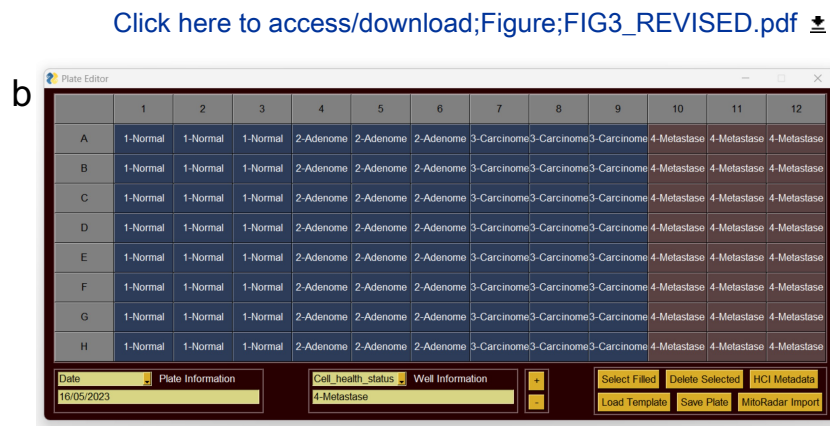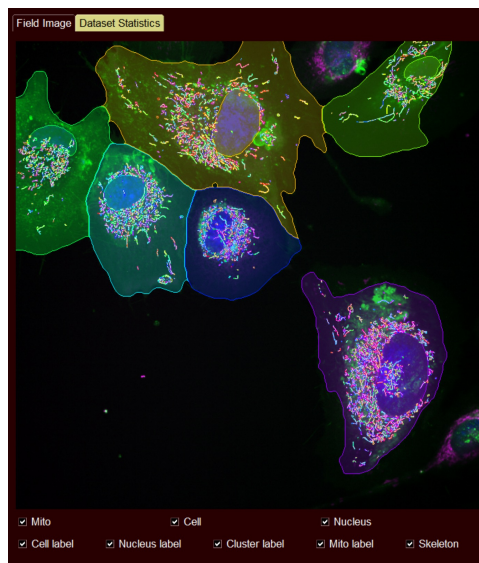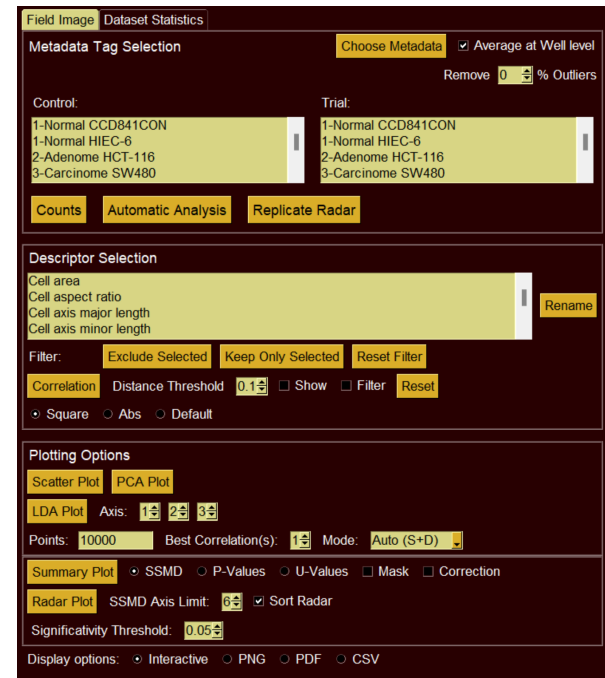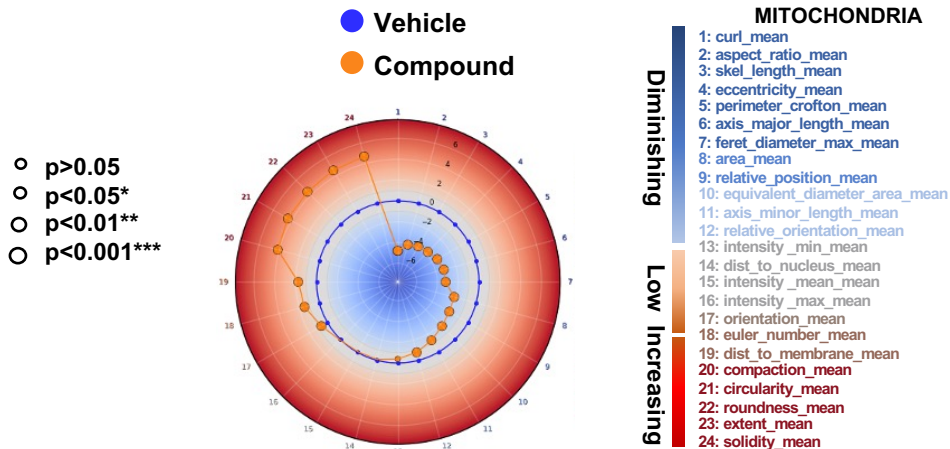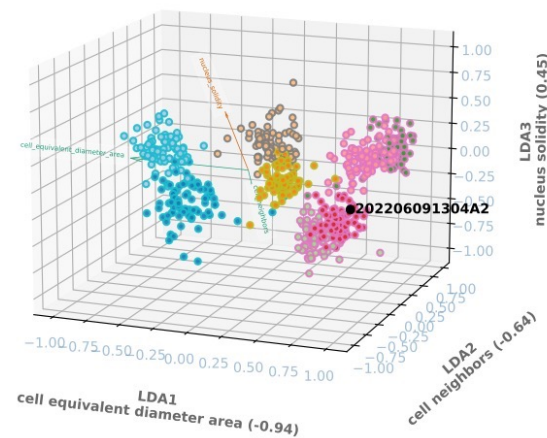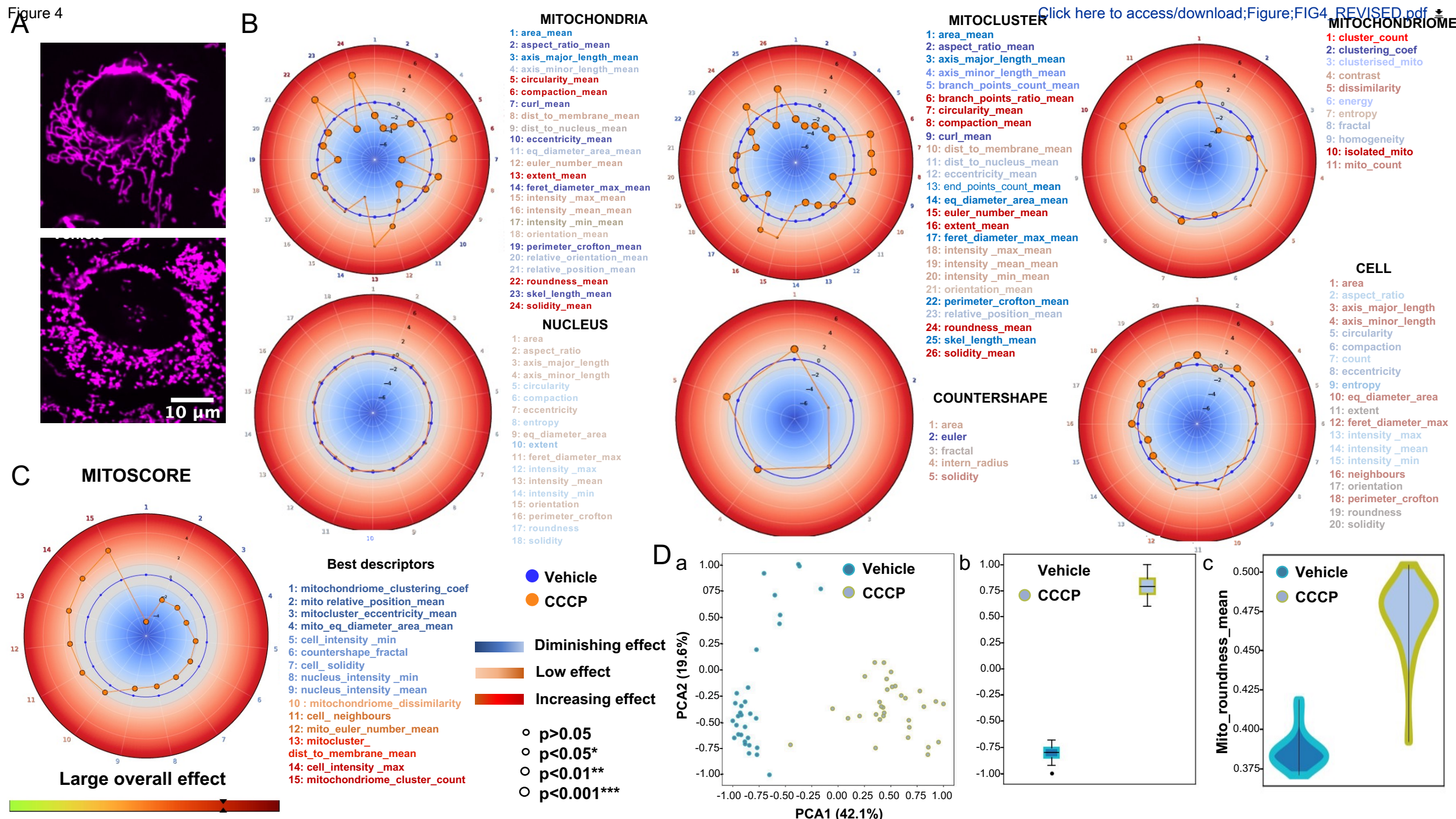
PESTICIDES	CATEGORY	THRESHOLD DOSE	LD50
FENPYROXIMATE	ACARICIDE	50µM	>500µM
PYRIDABEN	ACARICIDE	50µM	>500µM
MEPRONIL	FONGICIDE	50µM	≥ 500µM
THIFLUZAMIDE	FONGICIDE	10µM	100µM
AZOXYSTROBIN	FONGICIDE	100µM	≥ 500µM
PYRACLOSTROBIN	FONGICIDE	10µM	>500µM

C

overall effect

No
Limited
Measurable
Substantial
Large

D

LDA2
Mito euler number mean (0.67)

mito_euler_number_mean

mitocluster_skel_length_mean

LDA1
Mitocluster skel length mean (0.92)

- Vehicle
- CCCP
- Cpx I inhib FEN/PYRI
- Cpx II inhib MEP/THI
- Cpx III inhib AZO/PYRA

B

- Vehicle
- CCCP
- FEN
- PYRI
- MEP
- THI
- AZO
- PYRA

Diminishing effect
Low effect
Increasing effect

MITOCHONDRIA

1: area_mean
2: aspect_ratio_mean
3: axis_major_length_mean
4: axis_minor_length_mean
5: circularity_mean
6: compaction_mean
7: curl_mean
8: dist_to_membrane_mean
9: dist_to_nucleus_mean
10: eccentricity_mean
11: equivalent_diameter_area_mean
12: euler_number_mean
13: extent_mean
14: feret_diameter_max_mean
15: intensity _max_mean
16: intensity _mean_mean
17: intensity _min_mean
18: orientation_mean
19: perimeter_crofton_mean
20: relative_orientation_mean
21: relative_position_mean
22: roundness_mean
23: skel_length_mean
24: solidity_mean

MITOCLUSTER

1: area_mean
2: aspect_ratio_mean
3: axis_major_length_mean
4: axis_minor_length_mean
5: branch_points_count_mean
6: branch_points_ratio_mean
7: circularity_mean
8: compaction_mean
9: curl_mean
10: dist_to_membrane_mean
11: dist_to_nucleus_mean
12: eccentricity_mean
13: end_points_count_mean
14: equivalent_diameter_area_mean
15: euler_number_mean
16: extent_mean
17: feret_diameter_max_mean
18: intensity _max_mean
19: intensity _mean_mean
20: intensity _min_mean
21: orientation_mean
22: perimeter_crofton_mean
23: relative_position_mean
24: roundness_mean
25: skel_length_mean
26: solidity_mean

MIITOCHONDRIOME

1: cluster_count
2: clustering_coef
3: clusterised_mito
4: contrast
5: dissimilarity
6: energy
7: entropy
8: fractal
9: homogeneity
10: isolated_mito
11: mito_count

- p>0.05
- p<0.05*
- p<0.01**
- p<0.001***

Figure 6

A

PESTICIDES	CATEGORY	THRESHOLD DOSE	LD50
FOLPEL	FONGICIDE	50µM	150µM
PENDIMATHALINE	HERBICIDE	250µM	>500µM
CHLORPYRIPHOS	FONGICIDE	50µM	100µM
LINDANE	INSECTICIDE	500µM	500µM
CYPRODINIL	FONGICIDE	100µM	75µM

B

DEPARTMENT	PESTICIDE COMBINATION	PERCENTAGE IN MIXTURE	THRESHOLD DOSE	LD50
TARN ET GARONNE	PENDIMATHALINE	83%	50µM	100µM
	FOLPEL	8%	4,8µM	9,6µM
	LINDANE	6,5%	1,3µM	2,6µM
	CYPRODINIL	2,2%	3,9µM	7,8µM
PYRENEES-ORIENTALES	FOLPEL	88%	10µM	10µM
	PENDIMATHALINE	4%	0,47µM	0,47µM
	CHLORPYRIPHOS	4%	0,47µM	0,47µM
	CYPRODINIL	4%	0,47µM	0,47µM
LAURAGAIS	PENDIMATHALINE	78%	50µM	100µM
	FOLPEL	20%	13,3µM	27µM
	LINDANE	1,8%	1,2µM	2,4µM
AUDE	FOLPEL	97%	10µM	10µM
	PENDIMATHALINE	1,1%	0,11µM	0,11µM
	CHLORPYRIPHOS	0,8%	0,15µM	0,15µM
	LINDANE	1,5%	0,08µM	0,08µM
GARD	FOLPEL	93%	10µM	10µM
	PENDIMATHALINE	1,5%	0,2µM	0,2µM
	CHLORPYRIPHOS	5%	0,54µM	0,54µM

C

VEHICLE — PESTICIDE ALONE — AUDE PESTICIDES MIXTURE

a b FOL 10µM c FOL 50µM d MIX FOL 10µM

D

FOLPEL PESTICIDE ALONE

VEHICLE
FOL 10µM
FOL 50µM
FOL 100µM

MITOCHONDRIA
1: relative_position_mean
2: eccentricity_mean
3: dist_to_nucleus_mean
4: aspect_ratio_mean
5: skel_length_mean
6: perimeter_crofton_mean
7: axis_major_length_mean
8: feret_diameter_max_mean
9: area_mean
10: eq_diameter_area_mean
11: axis_minor_length_mean
12: curl_mean
13: intensity _max_mean
14: relative_orientation_mean
15: intensity _mean_mean
16: euler_number_mean
17: dist_to_membrane_mean
18: orientation_mean
19: intensity _min_mean
20: solidity_mean
21: circularity_mean
22: extent_mean
23: roundness_mean
24: compaction_mean

AUDE PESTICIDES MIXTURE

VEHICLE
MIX FOL 10µM
MIX FOL 50µM
MIX FOL 100µM

MITOCHONDRIA
1: aspect_ratio_mean
2: eccentricity_mean
3: skel_length_mean
4: axis_major_length_mean
5: feret_diameter_max_mean
6: relative_position_mean
7: perimeter_crofton_mean
8: area_mean
9: eq_diameter_area_mean
10: dist_to_nucleus_mean
11: intensity _max_mean
12: axis_minor_length_mean
13: intensity _mean_mean
14: relative_orientation_mean
15: dist_to_membrane_mean
16: intensity _min_mean
17: solidity_mean
18: euler_number_mean
19: orientation_mean
20: circularity_mean
21: curl_mean
22: extent_mean
23: roundness_mean
24: compaction_mean

E

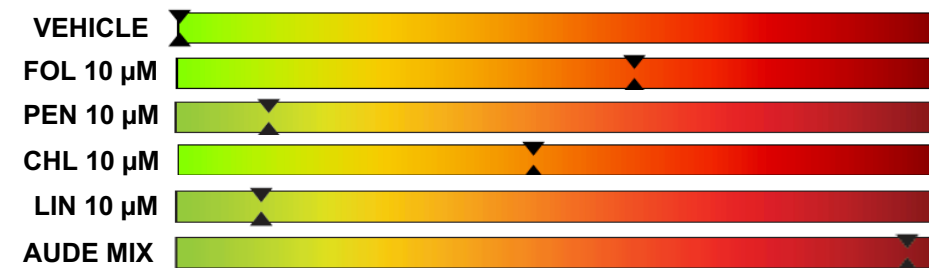

VEHICLE
FOL 10 µM
PEN 10 µM
CHL 10 µM
LIN 10 µM
AUDE MIX

Declarations of interest: none.

Sophie Charrasse: Data curation; formal analysis; investigation; visualization; methodology; writing – review and editing.

Charlotte Saint-Omer: Data curation; formal analysis; investigation; visualization; methodology.

Benoît Bordignon: Data curation; formal analysis; investigation; visualization; methodology.

Manuela Pastore : Data curation; software; formal analysis; investigation; visualization; methodology; writing – review and editing.

Richard E. Frye : Resources; data curation; methodology; writing – review and editing.

Titouan Poquillon : Data curation; software; formal analysis; investigation; visualization; methodology; writing – review and editing.
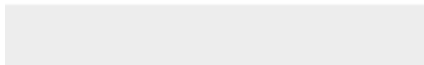
Victor Racine : Data curation; software; formal analysis; investigation; visualization; methodology; writing – review and editing.
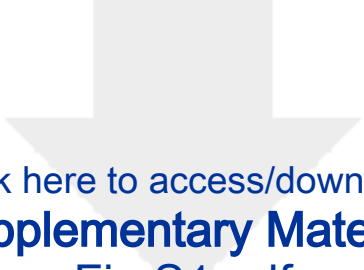
Christelle Reynes : Data curation; software; formal analysis; investigation; visualization; methodology; writing – review and editing.

Abdel Aouacheria: Conceptualization; data curation; formal analysis; supervision; funding acquisition; investigation; visualization; writing – original draft; project administration; writing – review and editing.
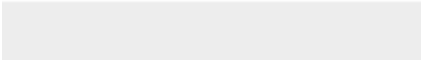
Table S1

Click here to access/download
Supplementary Material
Table S1.pdf

Figure S1

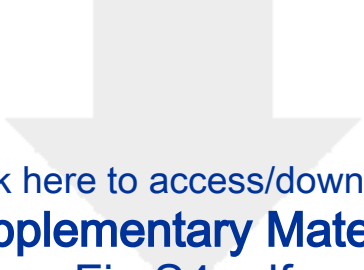Click here to access/download
Supplementary Material
Fig S1.pdf

Figure S2

Click here to access/download
Supplementary Material
Fig S2.pdf

Figure S3

Click here to access/download
Supplementary Material
Fig S3.pdf

Figure S4

Click here to access/download
Supplementary Material
Fig S4.pdf

Figure S5

Click here to access/download

Supplementary Material

FIG_S5_REVISED.pdf

Figure S6

Figure S7

Click here to access/download
Supplementary Material
FIG_S7_NEW.pdf